

5-2017

Integration of Macro-Fiber Composite Material on a Low Cost Unmanned Aerial System

May Chong Chan

Follow this and additional works at: <https://commons.erau.edu/edt>



Part of the [Aerospace Engineering Commons](#)

Scholarly Commons Citation

Chan, May Chong, "Integration of Macro-Fiber Composite Material on a Low Cost Unmanned Aerial System" (2017). *Dissertations and Theses*. 322.

<https://commons.erau.edu/edt/322>

This Thesis - Open Access is brought to you for free and open access by Scholarly Commons. It has been accepted for inclusion in Dissertations and Theses by an authorized administrator of Scholarly Commons. For more information, please contact commons@erau.edu.

INTEGRATION OF MACRO-FIBER COMPOSITE MATERIAL
ON A LOW COST UNMANNED AERIAL SYSTEM

A Thesis

Submitted to the Faculty

of

Embry-Riddle Aeronautical University

by

May Chong Chan

In Partial Fulfillment of the

Requirements for the Degree

of

Master of Science in Aerospace Engineering

May 2017

Embry-Riddle Aeronautical University

Daytona Beach, Florida

INTEGRATION OF MACRO-FIBER COMPOSITE MATERIAL
ON A LOW COST UNMANNED AERIAL SYSTEM

by

May Chong Chan

A Thesis prepared under the direction of the candidate's committee chairman, Dr. Hever Moncayo, Department of Aerospace Engineering, and has been approved by the members of the thesis committee. It was submitted to the School of Graduate Studies and Research and was accepted in partial fulfillment of the requirements for the degree of Master of Science in Aerospace Engineering.

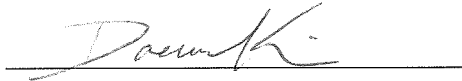
THESIS COMMITTEE



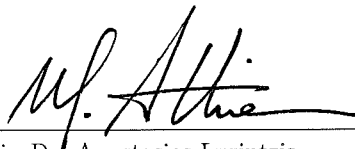
Chairman, Dr. Hever Moncayo



Member, Dr. Richard Prazenica



Member, Dr. Daewon Kim



Department Chair, Dr. Anastasios Lyrantzis
or Graduate Program Coordinator, Dr. Magdy Attia

4.18.2017
Date



Dean of College of Engineering, Dr. Maj Mirmirani

4/20/2017
Date



Vice Chancellor, Academic Support, Dr. Christopher Grant

4/20/17
Date

ACKNOWLEDGMENTS

I would never have been able to complete my thesis without the guidance of my advisory committee, the financial support from my sponsor, research projects, and the university, the help from my friends, as well as, the love of my family. Immeasurable appreciation and the deepest gratitude to everyone for their support and for the pleasant work climate.

Specifically, I wish to thank Dr. Moncayo for his continuous guidance, encouragement, and help through these three years and for giving me the opportunity to work in diverse projects that help me grow as a person and as an engineer. I would also like to thank the members of my thesis committee, Dr. Prazenica and Dr. Kim, for their constant feedback of ideas and advice for the thesis. Special thanks to Andres Perez, Boutros Azizi, Matt Clark, Lenny Gartenberg, Tony Zhao, and Agustin Giovagnoli for their much appreciated assistance.

TABLE OF CONTENTS

	Page
LIST OF TABLES	vi
LIST OF FIGURES	vii
ABBREVIATIONS	x
ABSTRACT	xi
1 Introduction	1
1.1 Objectives	5
1.2 Publications	6
2 Aileron Actuator Design	7
2.1 Modeling and Design	7
2.1.1 Analytical Theory	9
2.2 Experimental Setup	12
2.3 Fabrication	13
2.3.1 Wind Tunnel Testing	15
3 Simulation Environment	19
3.1 Aircraft Model	20
3.1.1 Aircraft Parameters	20
3.1.2 Trim Condition	20
3.2 Actuator Model	24
3.2.1 Engine Model	28
3.3 Sensor Model	29
3.4 Visualization	30
4 Control Law Design	32
4.1 Aircraft Dynamics	32
4.1.1 Linearization of the Skywalker Model	32
4.1.2 Poles for the Open-Loop System	39
4.1.3 Aircraft Dynamic Behavior through Transfer Function	40
4.2 Control Laws	41
4.2.1 Model Reference Adaptive Control (MRAC)	41
4.3 Linear Quadratic Regulator (LQR)	45
4.4 Waypoint Navigation	47
5 Performance Evaluation	51

	Page
5.1 Performance Metrics	52
5.2 Actuator Performance Analysis	56
6 System Integration for Future Development	62
6.1 Hardware Integration	63
6.1.1 Instrumentation	64
6.1.2 AMT2012-CE3 Dual High Voltage Amplifier	69
6.2 Software Integration	70
6.2.1 Simulink Models	70
6.2.2 Signal Conversion	72
7 Conclusion and Recommendation	75
REFERENCES	77
A Skywalker Pre-flight Checklist	78

LIST OF TABLES

Table	Page
2.1 Geometric and Material Properties for the MFC Actuators	14
3.1 Main Characteristics of Skywalker 1880 Airframe	21
3.2 Original Aircraft Stability and Control Derivatives	22
3.3 Lift and Drag Coefficients Comparison Between Mechanical and MFC-Actuated Ailerons Simulation	24
3.4 Aircraft Trim Condition for Mechanical and MFC-Actuated Ailerons Simulation	25
3.5 Specification for Mechanical Servo	27
4.1 Poles for Longitudinal Modes of the Skywalker	39
4.2 Poles for Lateral Modes of the Skywalker	39
5.1 Performance Index Weight and Normalization Cut-off Values for Trajectory Tracking	56
5.2 Performance Index Weight and Normalization Cut-off Values for Control Activity	57

LIST OF FIGURES

Figure	Page
1.1 Material structure of MFC	5
2.1 Theoretical Tip Displacement Comparison Between Unimorph and Bimorph Structures Using Different Substrate Materials	10
2.2 Theoretical Unimorph and Bimorph Actuator Deflections Corresponding to Substrate Thickness	11
2.3 Theoretical Blocking Force for Unimorph MFC Actuator Corresponding to Actuator Width	12
2.4 Experimental Setup for Unimorph and Bimorph Actuator Bench Test .	13
2.5 Theoretical and Experimental Deflection Comparison	14
2.6 MFC Aileron Design	16
2.7 Wind Tunnel Test Setup for Unimorph MFC Aileron	17
2.8 Wind Tunnel Test Results for Bimorph MFC Aileron	17
2.9 Wind Tunnel Test Results for Unimorph MFC Aileron	18
3.1 Overview of MRAC Simulated Model	19
3.2 Geometry Measurement of Skywalker 1880 in Inches	23
3.3 Resultant Geometry in Tornado VLM	24
3.4 P.I.D. Servo Control Topology	25
3.5 Engine Model for Turnigy D3542/6 1000KV Brushless Outrunner Motor	29
3.6 Communication Between Simulink and FlightGear	30
3.7 Skywalker RC Model in FlightGear	31
3.8 Simple Graphical User Interface for the Simulation	31
4.1 Model Comparison between Simulated Linear and Nonlinear Dynamics	36
4.2 Pitch Response between Linear and Nonlinear Models	37
4.3 Bank Response between Linear and Nonlinear Models	38
4.4 Overview of MRAC Simulated Model	41

Figure	Page
4.5 Systems Output and Error Tracking of Regular Plant	43
4.6 Tracking Error Comparison Between Nominal and Disturbed Flights	44
4.7 Outer Loop Controller using LQR	47
4.8 Controller Response to Commands	48
4.9 Bearing Calculation Derivation for Waypoint Navigation	48
4.10 Waypoint Navigation Logic Implementation with Mechanical Actuator	50
4.11 Waypoint Navigation Logic Implementation with MFC Actuator	50
5.1 Navigation Flight Path	51
5.2 Trajectory Tracking	58
5.3 Control Activity	58
5.4 Performance Index Summary for Oval Path	59
5.5 Performance Index Summary for Figure-8 Path	60
5.6 Trajectory Tracking for Oval Path Using MFC-Actuated Ailerons	61
6.1 Skywalker 1880 Assembled RC Model with MFC Halved-Ailerons	62
6.2 Overview of Hardware Integration in the Skywalker 1880	63
6.3 APM 2.6 Overview	64
6.4 InvenSense MPU-6000	65
6.5 MediaTek MT3329	65
6.6 MS5611-01BA093 Barometric Pressure Sensor	66
6.7 Pitot Tube and Pressure Sensor	66
6.8 XBee Transceiver Module	67
6.9 Spektrum DX8 Transmitter and Receiver	68
6.10 Turnigy Brushless Motor	68
6.11 Turnigy 5000mAh Lipo Battery	69
6.12 AMT2012-CE3 Amplifier	70
6.13 Overview of APM-integrated Simulink Model	71
6.14 APM 2.0 Blockset in the Simulink Library	72
6.15 Simulink Sensor Model	73

Figure	Page
6.16 Switch Command between Mechanical and MFC Ailerons	73
6.17 PWM-to-Voltage Conversion	74
7.1 Proposed Design for MFC-Actuated Ailerons	76

ABBREVIATIONS

AOA	Angle-of-Attack
6-DOF	six Degree-of-Freedom
MFC	Macro-Fiber Composite
PID	Proportional, Integral, and Derivative
UAV	unmanned aerial vehicle
MRAC	Model Reference Adaptive Control
LQR	Linear Quadratic Regulator
APM	ArduPilot Mega
DAS	Data Acquisition System
DC	Direct Current
CAD	Computer-Aided Design
PIV	Proportional-Integral-Velocity
PWM	Pulse-Width Modulation
GPS	Global Positioning System
RC	Radio-Controlled
ESC	Electronic Speed Controller
BEC	Battery Eliminator Circuit
NASA	National Aeronautics and Space Administration
ERAU	Embry-Riddle Aeroanautical University
in	inches
ft	feet
mph	miles per hour

ABSTRACT

Chan, May Chong MSAE, Embry-Riddle Aeronautical University, May 2017. Integration of Macro-Fiber Composite Material on a Low Cost Unmanned Aerial System.

The development, deployment, and operation of Unmanned Aerial Systems (UAS) have grown exponentially in recent years and have provided researchers with the opportunity to gain hands-on experience with aircraft in a manner that was previously limited to institutions and companies with large budgets. This allows the generation and testing of UAS advanced technologies using low cost systems. The scope of this thesis does not aim to make vast improvements to the control strategy itself, but to expand upon previous UAV work carried out at Embry-Riddle by designing, implementing, and demonstrating a simulation environment for mechanical and Macro-Fiber Composite (MFC) actuated ailerons in a Skywalker 1880 UAV using model reference adaptive control law. This work will contribute to a baseline model for the research and development of future UAV with morphing control surfaces up to a flight test stage. Meanwhile the extensive use of low-cost hardware and open-source software allows the opportunity to explore the feasibility of using affordable open-source technology in an academic context. Future students who are interested in morphing designs for UAV may find the baseline system presented here to be a useful starting point from which to begin their own research.

1. Introduction

The dream of flying is probably as old as mankind itself. However, the concept of an aircraft has only been around for slightly over a century. Brilliant minds, such as Leonardo da Vinci, had attempted to navigate the air by imitating the birds. Da Vinci, perhaps, was the first European interested in practical solution to flight when he designed the human-powered ornithopter in 1485. This mechanical design was patterned after birds and was intended to fly using flapping mechanism. The device, while it seemed like a good plan, only works at bird scale. Anything at a larger scale to lift both human and machine off the ground, needs a redesign. So over the century, there were many attempts at constructing a machine that would sail the sky like how ships traverse the ocean. From flights in the 1783 Montgolfier hot-air-balloon to the 1874 Felix du Temple, they all ended up with woefully uncontrolled flights. However, on December 17, 1903, two brothers did what many had attempted yet failed. The Wright Flyer, with a canard biplane configuration, took its first controlled, sustained, and powered flight at Kitty Hawk, North Carolina.

Aircraft design has taken a huge leap since the Wright brothers first flight. From passenger aircraft to sleek, high-speed fighter jets, the requirements to increase aircraft size and their flight envelopes had pushed aerospace engineers to utilize hinged control surfaces and more rigid body materials such as metals in the airplane design

and manufacturing process. While the Wright brothers are credited with developing the first practical control surfaces, unlike the modern control surfaces that we are familiar with nowadays, they used wing warping. With close resemblance to the wings of modern birds, that were shaped by nature over 60 millions years of evolution, warping wings are undoubtedly the most efficient design for flights. Unfortunately, for man-built flying machines, the continual flexing of a wooden wing will quickly lead to structural failure. Therefore, in an attempt to rival the Wright brothers, Glenn Curtiss invented hinged wing control surface known as the aileron. Since then, aviation has been wedded to these hinged control surfaces that are known as ailerons, rudders, elevators, flaps, and spoilers when used on different lifting surfaces to help aircraft maneuver in particular directions. This active control method will be perfect if not for its tendency to create more drag and increase fuel consumption.

Another aspect of the aircraft design that affects its fuel consumption is the weight. Aluminum, the most commonly used material on modern aircraft, is ideal for manufacturing bigger and faster aircraft because of its strength, resistance to corrosion, and the lighter weight in comparison to other materials with similar properties. Even so, one of best-selling airplanes- Boeing's 737 Classic weighs at least 72,360lb at operating empty weight, with a 5,311USgal fuel capacity (StartupBoeing, StartupBoeingStartupBoeing2007).

This research is driven by fuel efficiency demands as the world begins to accost climate change. With aerospace conglomerates looking at ways reduce the industry's greenhouse gas emissions by building greener airplanes, the effort of this thesis is to

explore the feasibility of using morphing mechanism on control surfaces to minimize surface drag and to potentially reduce aircraft weight to help aircraft burn less fuel.

The flight test results for mechanical shape-adaptive wing from the collaboration between NASA and Flexsys have proven to reduce on long-ranged fixed wing aircraft up to 12-percent, and that represents large savings in fuel consumption (Flexsys, FlexsysFlexsys2017) . According to studies conducted by NASA Dryden Flight Research Center, a one percent reduction in drag for the U.S. fleet of wide-body transport aircraft could save approximately 200 million gallons of fuel per year (Creech, CreechCreech2012) . Current morphing structures, however, has several disadvantages, as it requires heavy motors, hydraulics, and structural reinforcement that lead to high complexity in structural design and expensive construction cost (Barbarino, Bilgen, Ajaj, Friswell, & Inman, Barbarino, Bilgen, Ajaj, Friswell, & InmanBarbarino et al.2011) . This in turn causes difficulty even in the smallest structural change in the system. The notion of using smart material with smooth curvature is to replace the current burdening structure and produce a lighter lifting surface for an unmanned aerial vehicle (UAV) with reduced drag. The smart material chosen for this research is the Macro Fiber Composite (MFC).

Developed at NASA Langley Research Center, the MFC is fabricated with piezo-fibers embedded in epoxy matrix and coated with Kapton skin(Center, CenterCenter2000). One of the main reasons MFC is chosen for this thesis is its flexibility. The flexibility of the material allows it to bond to curvaceous structures with ease, making it more applicable in real life than typical monolithic piezo-ceramic materials that has a

brittle material structure. Initially designed to be used on helicopter blades, aircraft wings, and for the shaping of aerospace structure, this low-cost piezoelectric device is often utilized for vibration, noise, and deflections control in composite beams and panels.

In more details, the MFC consists of rectangular piezoceramic rods laminated between layers of adhesive and polyimide film that contains electrodes that transfer applied voltages to and from the ribbon-shaped rods. There are two types of MFC - the P1 type, that is an elongator, that has a d33 operational mode, and the P2 type that utilizes a d31 operational mode, which makes it contractor. The d33 effect allows the elongators to extend up to 1800ppm when operated at the maximum voltage rate of -500V to +1500V, making them sensitive strain sensors. Whereas, the contractors with the d31 effect will contract up to 750ppm when operated at maximum voltage of -60V to +360V, and they are often used for energy harvesting and also as strain sensors (Corp., Corp.Corp.2017) . Figure 1.1 shows the material structure of the MFC.

This thesis presents the development of an UAV to support the design, testing and validation of macro-fiber composite based aileron actuators. MFC, which consist of piezoceramic fibers and electrodes embedded in an epoxy matrix, are an attractive choice for UAV actuation because they are manufactured as lightweight, thin sheets and, when implemented as bending actuators, can provide large structural deflections and high bandwidth. In this study, several aileron actuator designs were evaluated through a combination of theoretical and experimental analysis. The final configu-

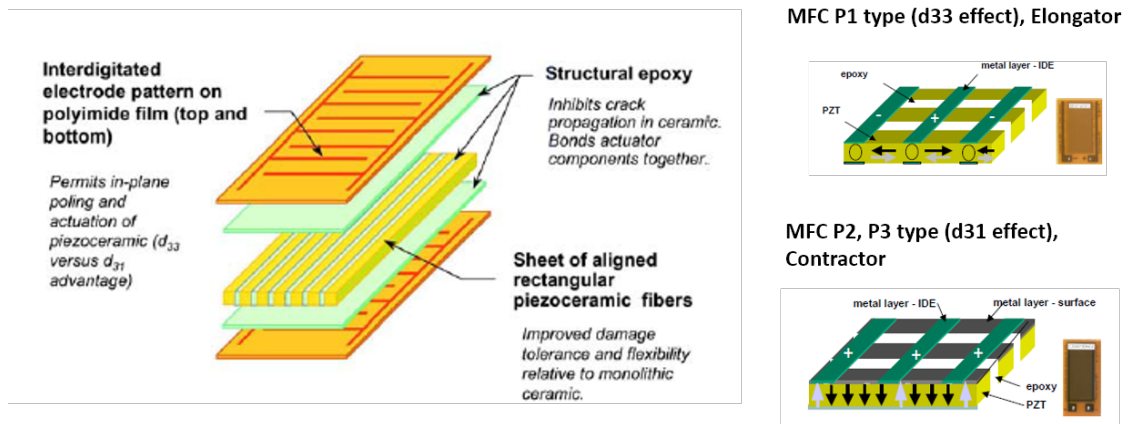


Figure 1.1. Material structure of MFC

ration is tested using in-flight data from a reduced size controlled research aircraft equipped with low cost autopilot and sensors package. The evaluation of the system is performed in terms of performance of the actuators to produce required roll control under different flight conditions.

1.1 Objectives

The objectives of this research are:

1. To develop unmanned aerial system and simulation development to support the design, testing, and validation of MFC-based aileron actuators.
2. To evaluate the aileron actuator designs through theoretical and experimental analysis.
3. To integrate MFC-based aileron actuation in a reduced-size controlled research aircraft equipped with low cost autopilot and sensor packaging.

1.2 Publications

The research effort presented in this thesis has resulted in the publication of:

1. Chan, M., Moncayo, H., Perez, A., Prazenica, R., Kim, D., Azizi, B., *Development and Flight Testing of an Unmanned Aerial System with Micro-Fiber Composite Actuators*, AIAA Infotech at Aerospace, AIAA Science and Technology Forum Orlando, FL., January 2015.
2. Prazenica, R., Kim, D., Moncayo, H., Azizi, B., Chan, M., *Design, Characterization, and Testing of Macro-Fiber Composite Actuators for Integration on a Fixed-Wing UAV*, Active and Passive Smart Structures and Integrated Systems VIII, SPIE Conference, March 2014.
3. Perez A. E., Moguel*I., Moncayo H., Chan C. May; *Low Cost Autopilot System for an Autonomous Unmanned Aerial System*, International Conference and Exhibition on Mechanical and Aerospace Engineering, Philadelphia, Pennsylvania, Sept. 2014.

2. Aileron Actuator Design

The design, modeling, and testing of the MFC actuator system was performed in collaboration with the ERAU Structures and Instrumentation Laboratory team. This section covers the modeling and design, analytical theory, experimental setup, fabrication, and wind tunnel testing of the MFC-actuators. These processes were carried out with the aim to improve the vehicle performance without affecting the structure integrity, stability, and control of the UAV. The main requirement for the aileron system actuation is to be able to move the aileron between ± 6 degree with a 0.1° accuracy. The controller must hold the aileron in place during the wind tunnel tests. As an important initial design decision, rather than attempting to embed the MFC actuators within the foam aileron, custom ailerons are fabricated for simpler implementation

2.1 Modeling and Design

Two designs were considered for the MFC ailerons - the unimorph and the bimorph actuators. The substrate material and thickness, blocking force, and predicted deflection based on voltage inputs were considered during the design process.

An MFC actuator mounted to an aileron substrate can be assumed to be a rigidly-supported cantilever beam. The deflection of a unimorph cantilever beam is given

as:(Gao, Shih, & Shih, Gao, Shih, & ShihGao et al.2009)(Wang & Cross, Wang & CrossWang & Cross1998)

$$\delta_{max} = -\frac{FL^3}{3wD_1} \quad (2.1)$$

where D_1 is the bending modulus per unit width, that can be expressed as

$$D_1 = \frac{E_s^2 t_s^4 + E_{MFC}^2 t_{MFC}^4 + 2E_s E_{MFC} t_s t_{MFC} (2t_s^2 + 2t_{MFC}^2 + 3t_s t_{MFC})}{12(E_s t_s + E_{MFC} t_{MFC})} \quad (2.2)$$

in which t_s is the thickness of the glass fiber substrate, E_s is the Young's Modulus of the glass fiber substrate, t_{MFC} is the thickness of the MFC, E_{MFC} is the tensile modulus of the MFC, w is the width of the unimorph actuator, L is the length of the MFC with F , equation 2.3, representing the blocking force at the tip of the beam

$$F = \frac{3wE_s t_s E_{MFC} t_{MFC} (t_s + t_{MFC})}{4L(E_s t_s + E_{MFC} t_{MFC})} d_{33} E_3 \quad (2.3)$$

where d_{33} is a constant representing the piezoelectric coupling effect with strain in the third direction. While, the electric field, E_3 , that is in the third direction is represented by equation 2.4:

$$E_3 = \frac{V_{app}}{t_{MFC}} \quad (2.4)$$

The parameters for these equations are t_s as the thickness of the glass fiber substrate, E_s as the Young's Modulus of the glass fiber substrate, t_{MFC} as the thickness

of the MFC, E_{MFC} as the Tensile Modulus of the MFC, w as the width of the actuator, F as the MFC blocking force, L as the length of the MFC, and v_{app} as the applied voltage.

Unlike the unimorph design, the bimorph actuator is composed of uniform substrate with the MFC mounted on the top and the bottom of the actuators. It can be modeled as a rigidly-supported, three-layer cantilever beam (Wang & Cross, Wang & Cross Wang & Cross 1999)

$$\delta = \frac{6s_{11}^s d_{33}(t_s + t_{MFC})L^2}{2s_{11}^s(3t_s^2 t_{MFC} + 6t_s t_{MFC}^2 + 4t_{MFC}^3) + s_{11}^{MFC} t_s^3} V \quad (2.5)$$

where

$$S_{11}^s = \frac{1}{E_s} \quad (2.6)$$

is the elastic coefficient of the supporting layer ($\frac{m^2}{N}$) and

$$S_{11}^{MFC} = \frac{1}{E_{MFC}} \quad (2.7)$$

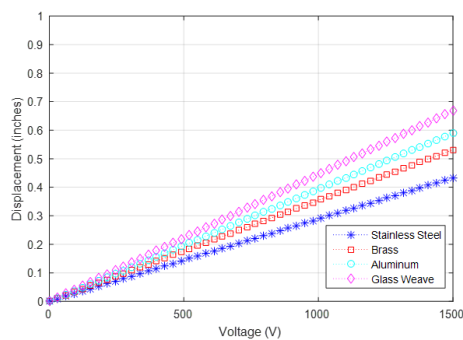
is the elastic coefficient of the piezoelectric layer ($\frac{m^2}{N}$).

2.1.1 Analytical Theory

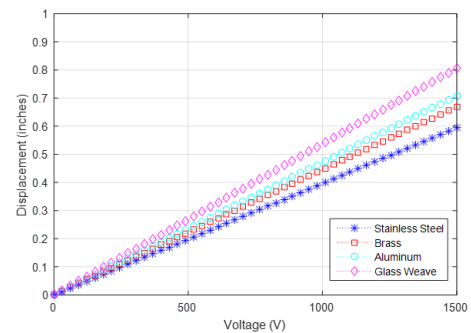
Instead of redesigning the ailerons on UAV for MFC application, aileron actuators made of MFC embedded onto substrate layers are used to move the ailerons. There are

two main considerations when it comes to material selection, the substrate materials and its thickness, that will affect the deflection efficiency of the ailerons.

Among the materials that have been considered for both of the designs are glass weave composite, aluminum, brass, and stainless steel. The theoretical actuator deflection angles for both of the designs using different materials are tabulated with their corresponding voltage inputs, and presented in Figure 2.1:



(a) Unimorph Actuator



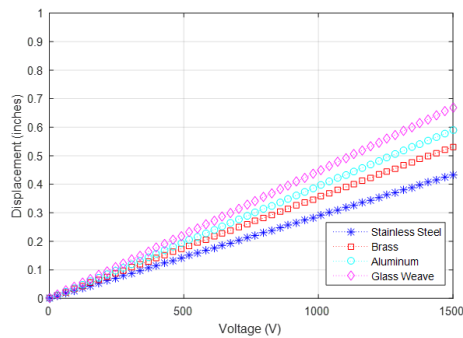
(b) Bimorph Actuator

Figure 2.1. Theoretical Tip Displacement Comparison Between Unimorph and Bimorph Structures Using Different Substrate Materials

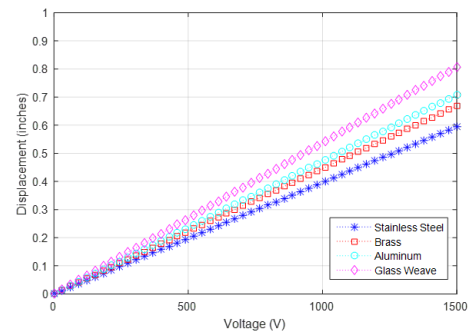
From Figure 2.1, all of the materials used for the both of the mentioned designs have a linear correlation between the voltage inputs and the deflection outputs. The bimorph design, due to its use of double layer MFC that collaborates to create bidirectional deflections, is expected to show larger deflection angles when compared to the unimorph actuator. As the other variables remain constant, the Young's Modulus of the substrates play a crucial role in affecting the amount of achievable actuator de-

flection. Glass weave substrate, with the lowest Young's Modulus, shows the largest calculated deflection in comparison to other chosen materials, and thus, is chosen for the experiments performed within this research.

Once the material has been selected, the next core factor that determines the deflection numbers, substrate thickness, is analyzed.



(a) Unimorph Actuator



(b) Bimorph Actuator

Figure 2.2. Theoretical Unimorph and Bimorph Actuator Deflections Corresponding to Substrate Thickness

From the theoretical model, unimorph MFC actuator displays an almost logarithmic increase in deflection for substrate thickness up to 0.0066in before an almost linear decline. This unexpected trend could be an attribute of the fact that a unimorph MFC actuator without substrate will elongate with the voltage applied, causing a bending moment on the structure that eventually leads to an increase in deflection, until the thickness of the substrate that affects the mass of the structure exceeds the blocking force of the MFC actuator itself, causing the unimorph actuator to reduce its

deflection. In contrast, the bimorph actuator has a monotonically decreasing angles of deflection as the substrate thickness increases, as expected.

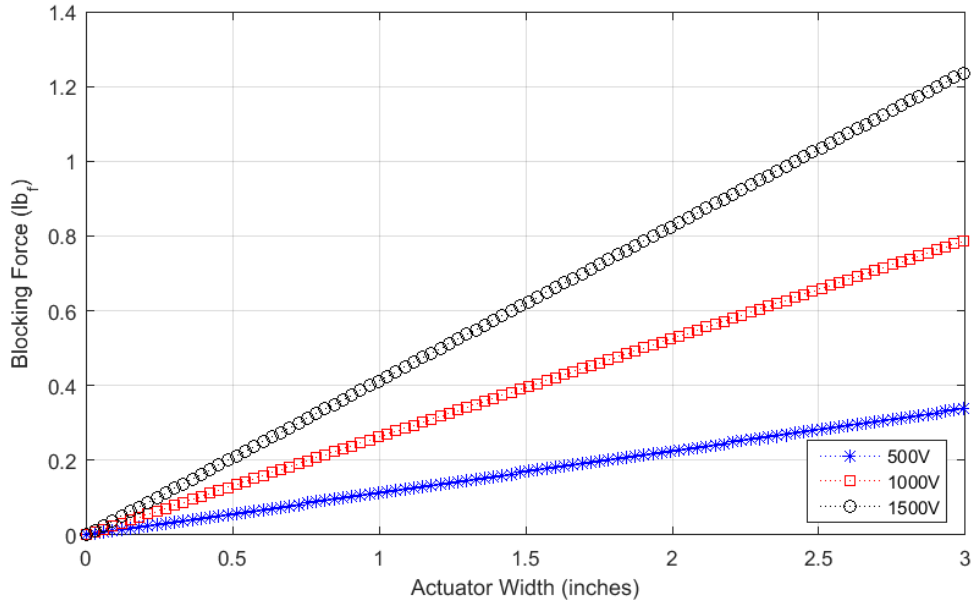
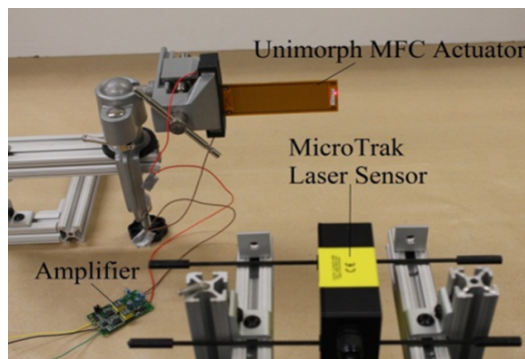


Figure 2.3. Theoretical Blocking Force for Unimorph MFC Actuator Corresponding to Actuator Width

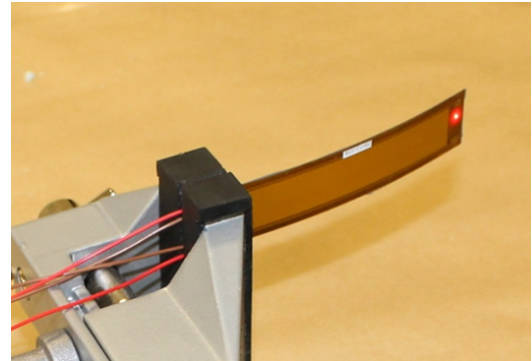
2.2 Experimental Setup

In order to verify the calculated values shown in the sections before, a series of experiments were conducted. The test environment includes DC power supply, high-voltage AMD2012CE3 amplifier, MicroTrak laser sensor, and a Data Acquisition System (DAS) running LabVIEW software. With a voltage supply ranging between 0 to 5V, the amplifier amplifies the voltage to a range of -500 to 1500V to actuate the MFC. The tip deflection is then measured by the MicroTrak laser sensor. As the

voltage input is regulated by the DAS, the MFC contracts between -500V to 0V and extends between 0.1V to 1500V, reaching a maximum deflection at 1500V.



(a) Experimental Setup



(b) Bimorph Actuator Testing

Figure 2.4. Experimental Setup for Unimorph and Bimorph Actuator Bench Test

2.3 Fabrication

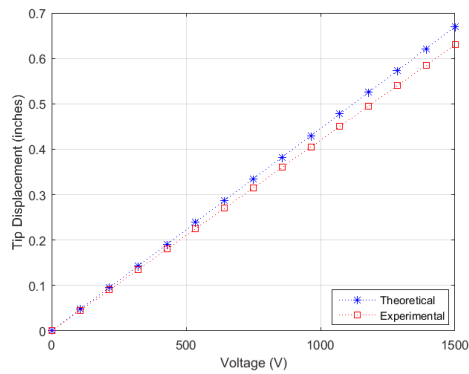
Based on the theoretical results, the unimorph and bimorph MFC actuators are fabricated with the dimensions and properties shown in Table 2.1:

For both of the designs, the MFCs are attached to the glass weave substrate using M-Bond 200 epoxy. Only the edges and parts of the MFC surface are embedded onto the substrate to allow the smart material to extend and contract in order to maximize the deflection angles of the actuator. The experimental results are illustrated in Figure 2.5(a) and 2.5(b).

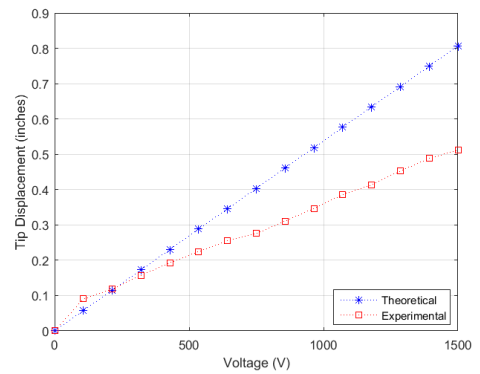
The experimental results from the graphs show a highly accurate theoretical prediction for unimorph actuator deflection, whereas the experimental result for bimorph

Table 2.1. Geometric and Material Properties for the MFC Actuators

Parameter	Unit	Value
MFC Dimensions ($L \times W \times t_{MFC}$)	in.	$3.35 \times 1.10 \times 0.012$
MFC Piezoelectric Constant, d_{33}	C/lb_f	2.05×10^{-9}
MFC Tensile Modulus, $E_1 = E_{MFC}$	Pa	30.4×10^9
Glass Fiber Substrate Dimensions ($L \times W \times t_s$)	in.	$3.35 \times 1.10 \times 0.016$
Glass Weave Modulus of Elasticity, E_s	Pa	26×10^9



(a) Unimorph Actuator



(b) Bimorph Actuator

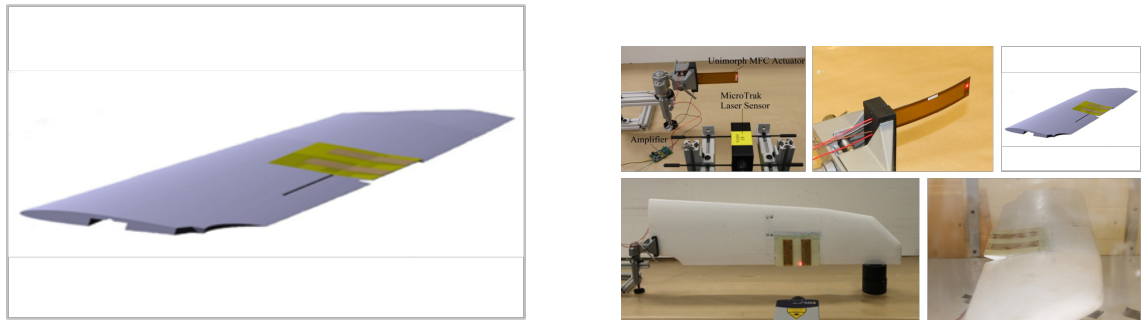
Figure 2.5. Theoretical and Experimental Deflection Comparison

actuator deflection display a reduction in actual deflection compared to its theoretical model. The unimorph actuator with a maximum tip deflection of more than 0.6in supersedes the bimorph actuator that has a maximum tip deflection of less than 0.5in.

2.3.1 Wind Tunnel Testing

The unimorph actuator design is selected focusing on the experimental results and application feasibility. Firstly, unimorph actuator generated more deflection when compared to bimorph actuator in experimental setup. Secondly, each of the MFC actuators requires an amplifier for operational purpose, thus using the unimorph design, does not only improve the deflection range, but also reduces the number of amplifiers from 8 to 4, which is a significant reduction in payload for the UAV. An additional benefit to utilizing the unimorph actuator is the fact that it allows the actuator to be employ to only half of the full-sized aileron while keeping the other half functioning as a backup mechanical aileron as a safety precaution in case of MFC aileron failure during flight.

The design, as depicted in Figure 2.6 , consists of two unimorph MFC actuators being mounted onto a sheet of glass weave substrate that is attached to the top of the foam aileron of the UAV. With this design, the MFC-actuated ailerons of the UAV, in contrast to conventional aileron design that deflects in both directions, is only capable of deflecting upwards. Therefore, the MFC-actuated ailerons generate roll in the UAV by decreasing the lift on one wing with its upward deflection to disrupt air flow over the wing surface, while maintaining the same lift on the other wing. The difference in lift on both of the wings, while not as significant as the mechanical ailerons, will still generate a rolling moment.



(a) CAD Model of Embedded MFC Actuator

(b) Bench Test Setup

Figure 2.6. MFC Aileron Design

Two layers of 0/90 cross-ply glass weave (Cycom 7701) were used for the construction of the aileron composite substrate. Layers of pre-peg fiberglass was cured in the oven to achieve a balanced combination of flexibility and durability. The sheet of MFC aileron is attached to the leading edge of the foam aileron using M-Bond 200 epoxy and the wiring to its amplifier were channeled through the wing spar towards the fuselage, where all the amplifiers reside.

The structure was tested in the university's low-speed wind tunnel, which has a 40in x 40in test section, with a flow speed of 28mph with a varying range within 2mph due to inconsistencies within the tunnel. Half a wing span was mounted on a force balance that is connected to a DAS to collect data.

Bimorph actuator was first tested in the wind tunnel at zero AOA. The results, as expected, shows a decrease in lift coefficient in a rather linear trend with respect to the increase in aileron deflection. Simultaneously, the drag coefficient exhibits a

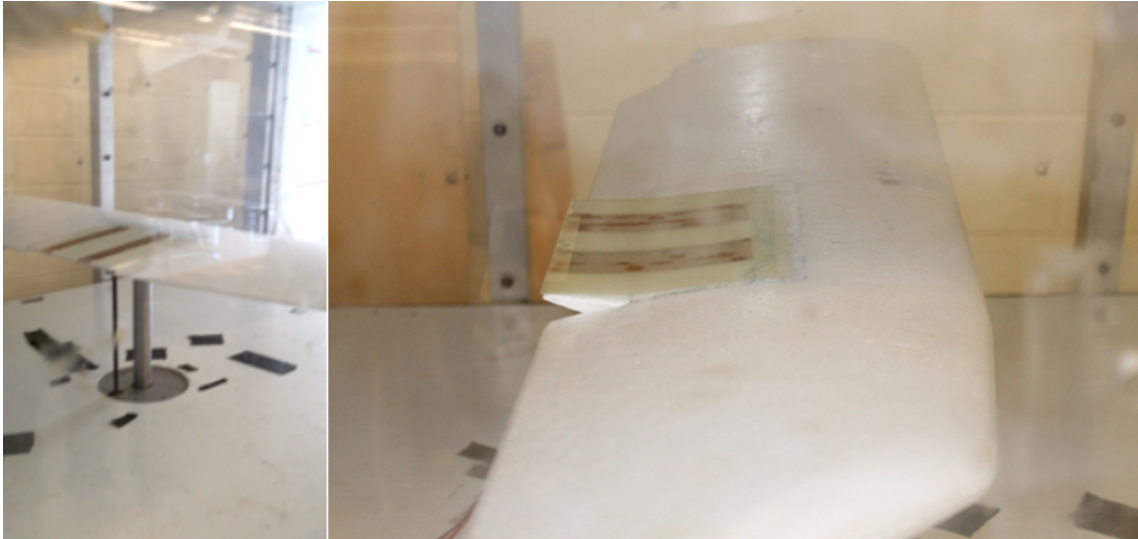
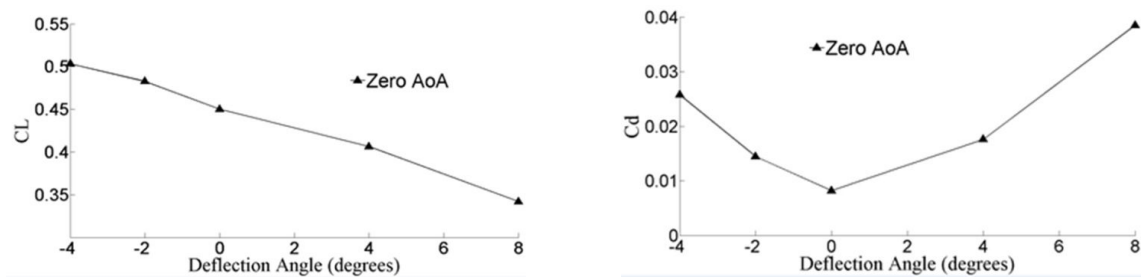


Figure 2.7. Wind Tunnel Test Setup for Unimorph MFC Aileron



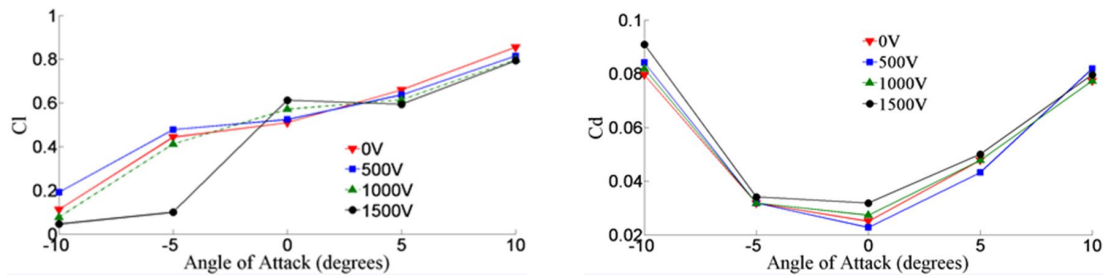
(a) Lift Coefficient vs. Aileron Deflection

(b) Drag Coefficient vs. Aileron Deflection

Figure 2.8. Wind Tunnel Test Results for Bimorph MFC Aileron

classical behavior of a parabolic graph, in which the minimum point of the graph happens at zero angle of aileron deflection. The results are depicted in Figure 2.8.

Next, the unimorph design was tested in the wind tunnel with varying AOA in addition to aileron deflection. The results are displayed in Figure 2.9.



(a) Lift Coefficient vs. Aileron Deflection

(b) Drag Coefficient vs. Aileron Deflection

Figure 2.9. Wind Tunnel Test Results for Unimorph MFC Aileron

Since there is no mean to directly measure the aileron deflection, the deflection angle is calculated based on the voltage input. As expected, with a fixed aileron deflection, the wing produced more lift as the angle-of-attack (AOA) increases. Likewise, the minimum drag is observed at zero AOA.

3. Simulation Environment

In order to study the actuator performance of the MFC-actuated ailerons and learn about the impact of the new design on the UAV, a simulation architecture is developed in a model-based design environment using Matlab and Simulink. Among the simulation models are the aircraft model, actuator model, engine model, sensor model, control model, and flight simulator blocks for visualization purposes. All of the models, besides the flight simulator blocks, utilize raw data collected from the actual hardware configuration that is used in the UAV. The overview of the simulation structure is shown in Figure 3.1.

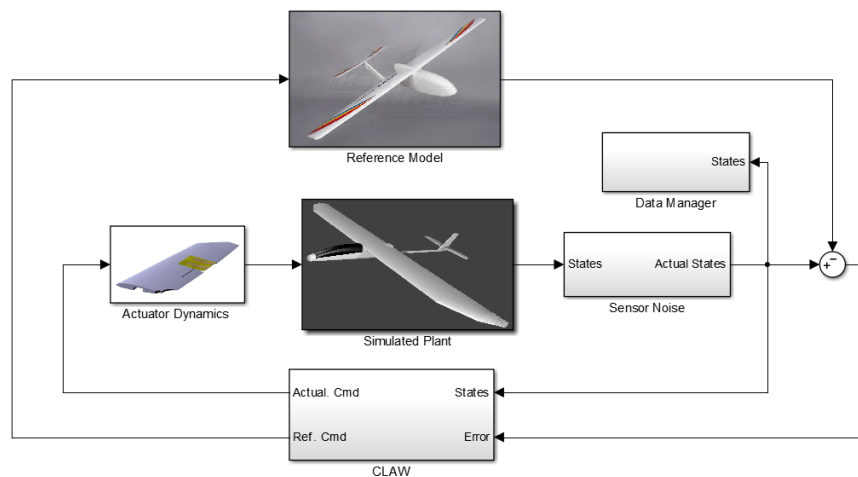


Figure 3.1. Overview of MRAC Simulated Model

3.1 Aircraft Model

The New Skywalker 1880 is chosen to serve as the testbed for this thesis based on its aircraft stability as a glider airplane and affordable cost. With a high wing, T-tail, pusher propeller configuration, it has an excellent lift-to-drag ratio that provides good gliding capabilities.

3.1.1 Aircraft Parameters

Most of the Skywalker parameters used to construct the aerodynamic model are obtained from previous works that includes only mechanically-actuated servo. They are displayed in Table 3.1, Figure 3.2, and Figure 3.3 (Chan et al., Chan et al. Chan et al.2014).

With the new MFC-actuated aileron design, new updates to the dynamic coefficients of the aircraft are incorporated into the simulation environment as tabulated below.

3.1.2 Trim Condition

A steady-state flight is crucial in providing initial condition for flight simulation. These condition data, including the initial velocity of the aircraft, trimmed thrust values, and elevator deflection at steady state, are produced using a generic trim program that is linked to a nonlinear Skywalker aircraft model.

Table 3.1. Main Characteristics of Skywalker 1880 Airframe

Parameter	Unit	Value
Wing Area	ft^2	4.424
Wing span	ft	6.168
Mean Aerodynamic Chord	ft	0.741
Total Length	ft	3.871
Weight	lb_f	2.100
J_{xx}	$lb \cdot ft^2$	2.326
J_{yy}	$lb \cdot ft^2$	3.370
J_{zz}	$lb \cdot ft^2$	5.933

Table 3.2. Original Aircraft Stability and Control Derivatives

Longitudinal			Lateral-Directional		
Coefficient	Value	Unit	Coefficient	Value	Unit
C_{L0}	0.251	N/A	$C_{Y\beta}$	-0.233	1/rad
$C_{L\alpha}$	5.421	1/rad	C_{Ydr}	0.0180	1/rad
C_{Lde}	0.551	1/rad	C_{Yp}	-0.108	1/(rad/sec)
C_{Lq}	10.22	1/(rad/sec)	C_{Yr}	0.208	1/(rad/sec)
C_{D0}	0.021	N/A	$C_{n\beta}$	0.100	1/rad
$C_{D\alpha}$	0.038	1/rad	C_{nda}	-0.005	1/rad
$C_{D\alpha^2}$	0.0878	1/rad ²	C_{ndr}	-0.058	1/rad
C_{Dde}	0.007	1/rad	C_{nr}	-0.090	1/(rad/sec)
C_{M0}	0.029	N/A	C_{np}	-0.035	1/(rad/sec)
$C_{M\alpha}$	-1.887	1/rad	$C_{l\beta}$	-0.034	1/rad
C_{Mde}	-1.872	1/rad	C_{lda}	-0.197	1/rad
C_{Mq}	-24.80	1/(rad/sec)	C_{ldr}	-0.004	1/rad
			C_{lp}	-0.529	1/(rad/sec)
			C_{lr}	0.025	1/(rad/sec)

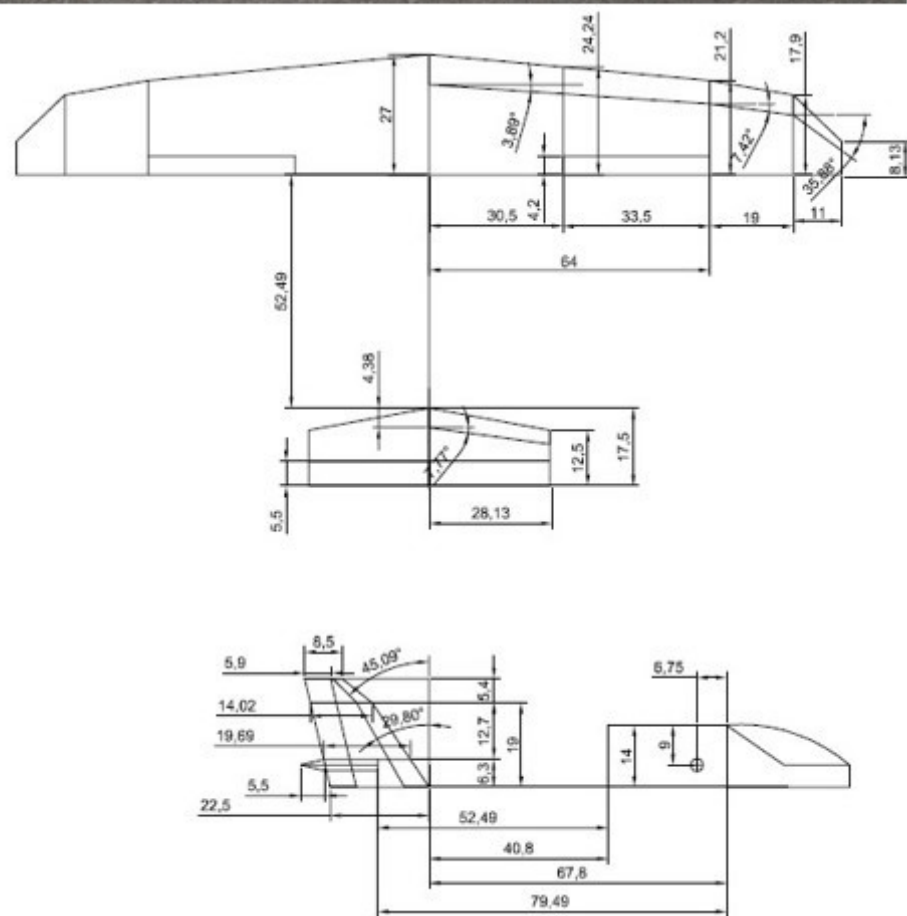


Figure 3.2. Geometry Measurement of Skywalker 1880 in Inches

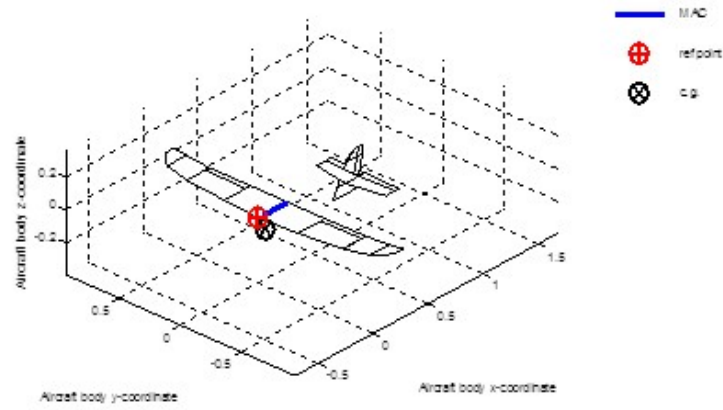


Figure 3.3. Resultant Geometry in Tornado VLM

Table 3.3. Lift and Drag Coefficients Comparison Between Mechanical and MFC-Actuated Ailerons Simulation

Coefficient	Mechanical Actuator	MFC Actuator
C_{L0}	0.251	0.49
$C_{L\alpha}$	5.421	2.292
C_{D0}	0.021	0.020
$C_{D\alpha^2}$	0.088	0.070

3.2 Actuator Model

The theory of servo motion control, that plays a significant role in controlling the actuators on the controls surfaces of an aircraft, has not undergone drastic changes in the last 50 years. The mechanical servo control in this thesis utilizes the disturbance rejection characteristics of the system through the use of a Proportional-Integral-Velocity (PIV) loop.

Table 3.4. Aircraft Trim Condition for Mechanical and MFC-Actuated Ailerons Simulation

Parameter	Unit	Mechanical Value	MFC Value
Initial Velocity	ft/s	70.0	71.17
Trimmed Thrust	lb_f	0.5118	0.0876
Steady-State Elevator Deflection	deg	-0.6118	0.1629

The mechanical actuator model utilizes standard Laplace notation. In their most fundamental form, mechanical servo drives, in the form of torque, T , is directly proportional to the voltage command, that is represented as the desired motor current, I , with a gain, K_t as listed in Equation 3.1.

$$T \approx K_t I \quad (3.1)$$

The servo drive closes this loop and is modeled as a linear transfer function, $G(s)$, as shown in Figure 3.4. While it is not entirely accurate due to the peak current limits in the servo drive, it offers a reasonable representation for our analysis.

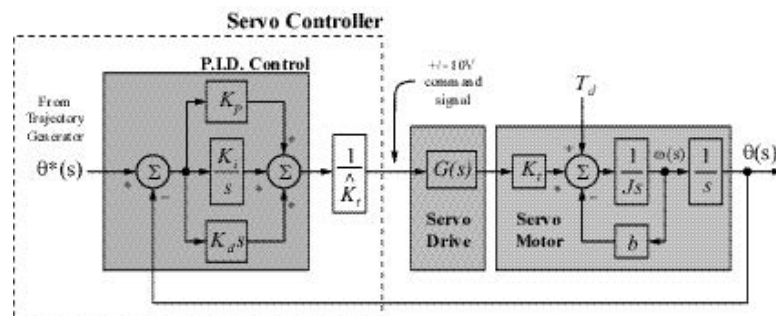


Figure 3.4. P.I.D. Servo Control Topology

The servomotor is modeled as a lump inertia, J , comprising both of the servomotor and load inertia, a viscous damping term, b , and a torque constant, K_t . In this model, the load is assumed to be rigidly coupled such that the torsional rigidity moves the natural mechanical resonance point beyond the bandwidth of the servo controller. This assumption simplifies the total system inertia to the sum of the motor and load inertia for the desired controllable frequencies.

Comparing the difference between the desired motor position, $\theta_d(s)$, and its actual position, $\theta(s)$, as shown in Equation 3.2, the Proportional-Integral-Derivative (PID) controller calculates the desired torque command based on the position error.

$$e(t) = \theta_d(t) - \theta(t) \quad (3.2)$$

The three gains of the PID controller, K_p , K_i , and K_d will act on the position error defined in Equation 3.3. The output of the PID controller is a torque signal that can be represented by this mathematical expression in the time domain

$$T_{out}(t) = K_p e(t) + K_i \int (e(t)) dt + K_d \frac{d}{dt} (e(t)) \quad (3.3)$$

In order to have a better prediction of the system response, a PIV controller is used. This controller combines the position loop with a velocity loop that allows for velocity correction command by multiplying the proportional gain with the position error. The integral gain in this model acts on the velocity error instead of the position error, as intended in the basic PID controller. The derivative gain is replaced by the velocity gain, K_v .

$$K_p = \frac{2\pi BW}{2\zeta + 1} \quad (3.4)$$

$$K_i = (2\pi BW)^2(1 + 2\zeta)\hat{J} \quad (3.5)$$

$$K_v = (2\pi BW)((1 + 2\zeta)\hat{J} - \hat{b}) \quad (3.6)$$

using an estimate of the motor's total inertia, \hat{J} , and damping, \hat{b} at initial set up. With an additional velocity input signal, only two control parameters are needed to tune this system: the bandwidth (BW) and the damping ratio (ζ). These values were obtained from previous work at the Flight Dynamics and Controls Research Laboratory, and are tabulated in Table 3.4(Hartley, Hugon, & DeRosa, Hartley, Hugon, & DeRosaHartley et al.2012).

Table 3.5. Specification for Mechanical Servo

Parameter	Unit	Left Aileron	Right Aileron	Elevator	Rudder
Bandwidth	rad/s	50.27	50.27	50.27	50.27
Servo Rate Limit	PWM	333.87	314.72	341.44	338.80
Max. Deflection	deg	19.89	23.77	28.08	28.91
Min. Deflection	deg	-27.52	-20.92	-19.80	-19.20

Since the mechanical and MFC-actuators utilize the same PWM input, the MFC-actuator uses the same actuator model with updates made to the maximum aileron deflection and aircraft's dynamic coefficient obtained from Chapter 2 of this thesis.

3.2.1 Engine Model

The raw data from the engine model, which includes force, motor current draw, and throttle positions, was acquired from previous engine modeling accomplished by ERAU researchers (Hartley et al., Hartley, Hugon, & DeRosaHartley et al.2012).

The pressure downstream of the engine, P_d , was derived from the basic pressure equation where the measured force, F_{meas} , is equivalent to the surface area of the propeller, S_{prop} , multiplied by pressure applied, in this case referring to the differential in pressure between P_d and the static pressure of the day, P_0 , as shown in Equation 3.7:

$$F_{meas} = S_{prop}(P_d - P_0) \quad (3.7)$$

By substituting the value of the downstream pressure into the Bernoulli's equation gives us

$$P_d = P_0 + \frac{1}{2}\rho V_e^2 \quad (3.8)$$

where the exit velocity, V_e , that is used to map throttle setting to exit velocity for a complete engine thrust model as described below.

$$F_T = \frac{1}{2}\rho S_{prop}(V_e^2 - V_T^2) \quad (3.9)$$

the predicted throttle force, F_T , is applied to the engine location that causes a negative pitching moment due to significant vertical offset with respect to the center of gravity. Figure 3.4 depicts the main block of the engine module for Turnigy D3542/6 1000KV Brushless Outrunner Motor.

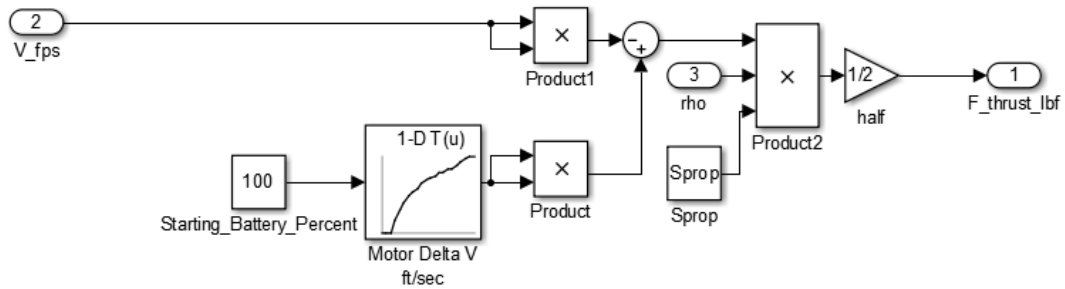


Figure 3.5. Engine Model for Turnigy D3542/6 1000KV Brushless Outrunner Motor

3.3 Sensor Model

Sensors, such as accelerometers and gyros, on-board of the Skywalker are modeled as white noise or as signals that follow a standard Gaussian distribution.

$$w(\mu, \sigma^2) = \frac{1}{\sqrt{2\pi\sigma^2}} e^{-\frac{(x-\mu)^2}{2\sigma^2}} \quad (3.10)$$

where x represents the input signal, μ represents mean of the signal, and σ represents standard deviation of the signal. The signal static bias and noise type were determined

in previous ERAU coursework through static analysis and frequency analysis using Fast Fourier algorithm.

3.4 Visualization

An open-source flight simulation software, known as FlightGear, is used for visualization purposes. As shown in Figure 3.6, the flight simulator is connected to the constructed Simulink model by utilizing the simulation blocks provided by Simulink's Flight Simulator Interfaces sub-library.

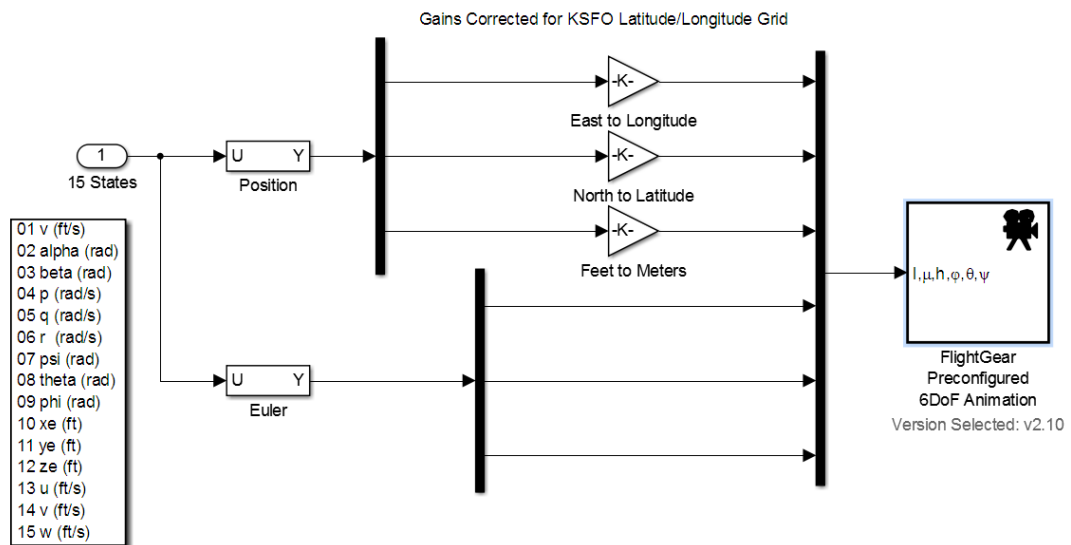


Figure 3.6. Communication Between Simulink and FlightGear

When provided with double-precision values for longitude (l), latitude (μ), altitude (h), roll (ϕ), pitch (θ), and yaw (ψ), the FlightGear Preconfigured 6DoF Animation block transfers and drives the position and attitude values to a FlightGear flight

simulator vehicle, in this case, a Skywalker UAV model that was built during a graduate-level course final project. The visualization results is shown in Figure 3.7.

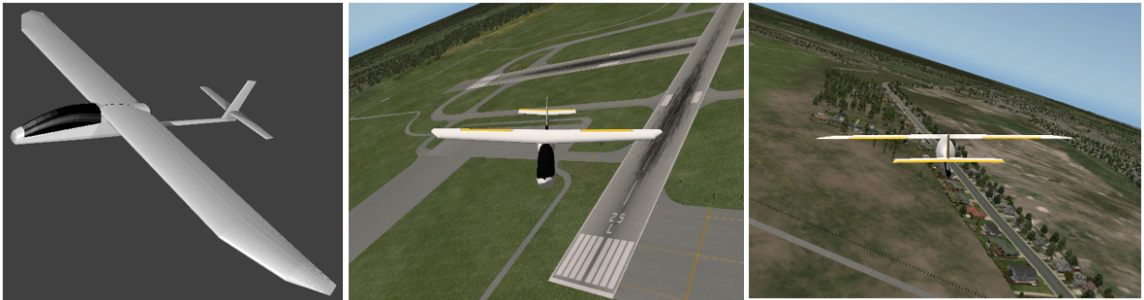


Figure 3.7. Skywalker RC Model in FlightGear

Furthermore, for the ease of execution for different simulation modes, an interactive user-interface was created to allow for ease of adding disturbances, such as abnormal control surfaces deflection angles, and switching between mechanical and MFC-actuated ailerons.

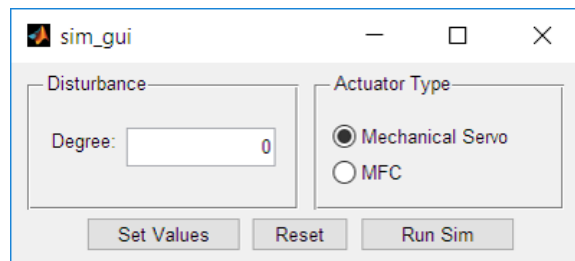


Figure 3.8. Simple Graphical User Interface for the Simulation

4. Control Law Design

In order to navigate through the referenced waypoints with minimal errors while taking into account the uncertainties in the aircraft due to the use of morphing MFC-actuated ailerons, the model reference adaptive controller (MRAC) in combination with a linear quadratic regulator (LQR) are used. This chapter focuses on explaining the role of aircraft dynamics in the controller design, and the design process of MRAC and LQR.

4.1 Aircraft Dynamics

The dynamic coefficients used in this section are mentioned in Chapter 3 regarding the simulation environment. In order to compare the controller performance between the mechanical and MFC actuators, two different sets of aircraft dynamics pertaining to each actuator setting are used in the model.

4.1.1 Linearization of the Skywalker Model

Under the condition of small perturbations from steady-state, wings-level, zero-sideslip flight, the aircraft equations of motion can be split into two uncoupled sets: longitudinal and lateral equations. Due to the limitations of the sensors feedback from the UAV, full state feedback is unachievable using the conventional linearized models.

Therefore, the aircraft architecture is carefully designed to accommodate the missing state feedbacks, while reducing redundant gains that will increase computational load.

Based on the feedback obtained from the sensors, which are loaded in the physical UAV, the longitudinal equations involve relative speeds in x- and z-directions, pitch attitude, and pitch rate.

$$\begin{aligned}
 \begin{bmatrix} \dot{u} \\ \dot{w} \\ \dot{\theta} \\ \dot{q} \end{bmatrix} &= \begin{bmatrix} X_u & X_w & -g\cos\theta_1 & -W_1 \\ \frac{Z_u}{Z_Z} & \frac{Z_w}{Z_Z} & -g\sin\theta_1 & \frac{Z_q+U_1}{Z_Z} \\ 0 & 0 & 0 & 1 \\ M_u + M_{\dot{w}}\frac{Z_w}{Z_Z} & M_w + M_{\dot{w}}\frac{Z_w}{Z_Z} & -\frac{M_{\dot{w}q}\sin\theta_1}{Z_Z} & M_q + \frac{M_{\dot{w}}}{Z_Z}(Z_q + U_1) \end{bmatrix} \begin{bmatrix} u \\ w \\ \theta \\ q \end{bmatrix} \\
 &+ \begin{bmatrix} -1.3606 \\ \frac{Z_{\delta_e}}{Z_Z} \\ 0 \\ M_{\delta_e} + \frac{M_{\dot{w}}Z_{\delta_e}}{Z_Z} \end{bmatrix} \delta_e \tag{4.1}
 \end{aligned}$$

For the aircraft model fitted with mechanical actuators, the longitudinal equations are

$$\begin{aligned}
 \begin{bmatrix} \dot{u} \\ \dot{w} \\ \dot{\theta} \\ \dot{q} \end{bmatrix} &= \begin{bmatrix} -0.4766 & 0.3037 & -32.1970 & 0.8082 \\ -1.1355 & -13.6480 & 0.4362 & 59.6612 \\ 0 & 0 & 0 & 1 \\ -0.2510 & -5.2807 & 0 & -18.4514 \end{bmatrix} \begin{bmatrix} u \\ w \\ \theta \\ q \end{bmatrix} + \begin{bmatrix} -1.3606 \\ -100.4368 \\ 0 \\ -292.0412 \end{bmatrix} \delta_e
 \end{aligned}$$

whereas the longitudinal equations for the aircraft model fitted with MFC actuator

are

$$\begin{bmatrix} \dot{u} \\ \dot{w} \\ \dot{\theta} \\ \dot{q} \end{bmatrix} = \begin{bmatrix} -0.6857 & -0.7131 & -31.6727 & 10.9318 \\ -1.5209 & -5.9550 & 5.8034 & 59.6612 \\ 0 & 0 & 0 & 1.0000 \\ 0.3863 & -5.1360 & 0 & -19.0817 \end{bmatrix} \begin{bmatrix} u \\ w \\ \theta \\ q \end{bmatrix} + \begin{bmatrix} -18.7078 \\ -102.0995 \\ 0 \\ -304.9991 \end{bmatrix} \delta_e$$

The lateral-directional equations involve relative speed in the y-direction, bank angle, as well as roll and yaw rates.

$$\begin{bmatrix} \dot{v} \\ \dot{\phi} \\ \dot{p} \\ \dot{r} \end{bmatrix} = \begin{bmatrix} Y_v & g \cos \theta_1 & W_1 + Y_p & Y_r - U_1 \\ 0 & 0 & 1 & \tan \theta_1 \\ L_v & 0 & L_p & L_r \\ N_v & 0 & N_p & N_r \end{bmatrix} \begin{bmatrix} v \\ \phi \\ p \\ r \end{bmatrix} + \begin{bmatrix} Y_{\delta_a} & Y_{\delta_r} \\ 0 & 0 \\ L_{\delta_a} & L_{\delta_r} \\ N_{\delta_a} & N_{\delta_r} \end{bmatrix} \begin{bmatrix} \delta_a \\ \delta_r \end{bmatrix} \quad (4.2)$$

The lateral equations for the aircraft model using mechanical actuator are

$$\begin{bmatrix} \dot{v} \\ \dot{\phi} \\ \dot{p} \\ \dot{r} \end{bmatrix} = \begin{bmatrix} -0.7412 & 32.1970 & -1.9209 & -68.0212 \\ 0 & 0 & 1 & 0 \\ -2.0280 & 0 & -34.3076 & 11.0751 \\ 1.2508 & 0 & 1.5862 & -4.0769 \end{bmatrix} \begin{bmatrix} v \\ \phi \\ p \\ r \end{bmatrix}$$

$$+ \begin{bmatrix} 0 & 29.3634 \\ 0 & 0 \\ -232.5938 & 17.9483 \\ 20.1128 & -54.4141 \end{bmatrix} \begin{bmatrix} \delta_a \\ \delta_r \end{bmatrix}$$

while the model for the one with MFC actuator is

$$\begin{bmatrix} \dot{v} \\ \dot{\phi} \\ \dot{p} \\ \dot{r} \end{bmatrix} = \begin{bmatrix} -0.7577 & 31.6727 & -13.8149 & -67.9885 \\ 0 & 0 & 1.0000 & -0.1832 \\ -2.0604 & 0 & -34.8756 & 11.2584 \\ 1.2716 & 0 & 1.6125 & -4.1444 \end{bmatrix} \begin{bmatrix} v \\ \phi \\ p \\ r \end{bmatrix} + \begin{bmatrix} 0 & 30.3437 \\ 0 & 0 \\ -240.3586 & 18.5475 \\ 20.7842 & -56.2307 \end{bmatrix} \begin{bmatrix} \delta_a \\ \delta_r \end{bmatrix}$$

To ensure sufficient accuracy of the derived linear models for controller design, outputs between the nonlinear and one of the linear aircraft models are compared and contrasted in Simulink as shown in Figure 4.1.

The graphs in Figures 4.2 and 4.3 show the comparison between the linear and nonlinear models for the longitudinal and lateral matrices, and as we can see, the linear model closely resembles the nonlinear model.

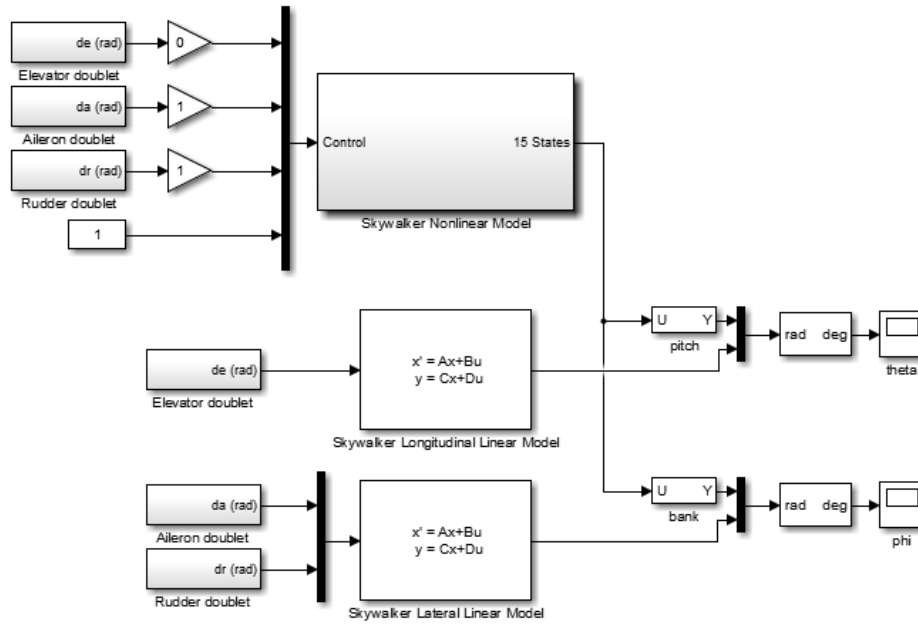


Figure 4.1. Model Comparison between Simulated Linear and Nonlinear Dynamics

Natural Frequencies for Longitudinal and Lateral Modes

The natural frequencies and damping ratio for both of the aircraft models are obtained through the constructed Simulink model. For the longitudinal mode, the natural frequencies, $\omega_{n,long}$, and damping ratio, ζ_{long} for mechanical and MFC actuators are

$$\omega_{n,long,mech} = \begin{bmatrix} 23.7174 \\ 23.7174 \\ 0.3776 \\ 0.3776 \end{bmatrix} \text{ rad/s}; \zeta_{long,mech} = \begin{bmatrix} 0.6757 \\ 0.6757 \\ 0.6519 \\ 0.6519 \end{bmatrix}$$

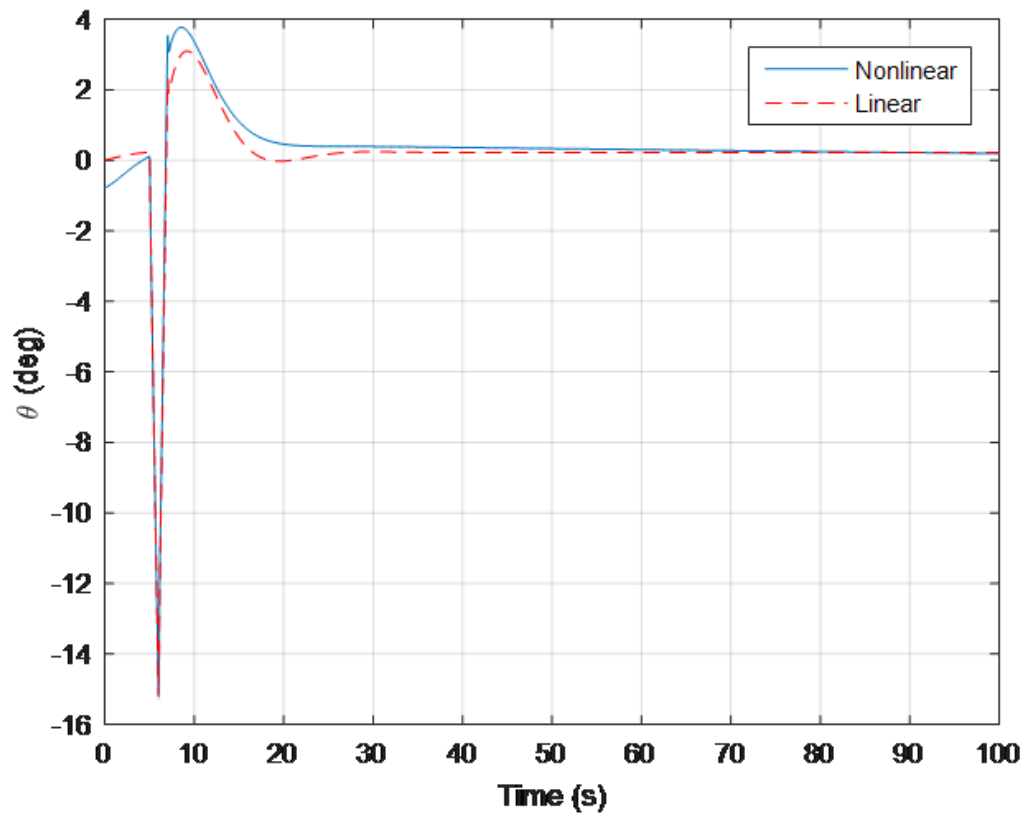


Figure 4.2. Pitch Response between Linear and Nonlinear Models

$$\omega_{n,long,MFC} = \begin{bmatrix} 20.4785 \\ 20.4785 \\ 0.9035 \\ 0.9035 \end{bmatrix} ; \zeta_{long,MFC} = \begin{bmatrix} 0.6167 \\ 0.6167 \\ 0.2569 \\ 0.2569 \end{bmatrix}$$

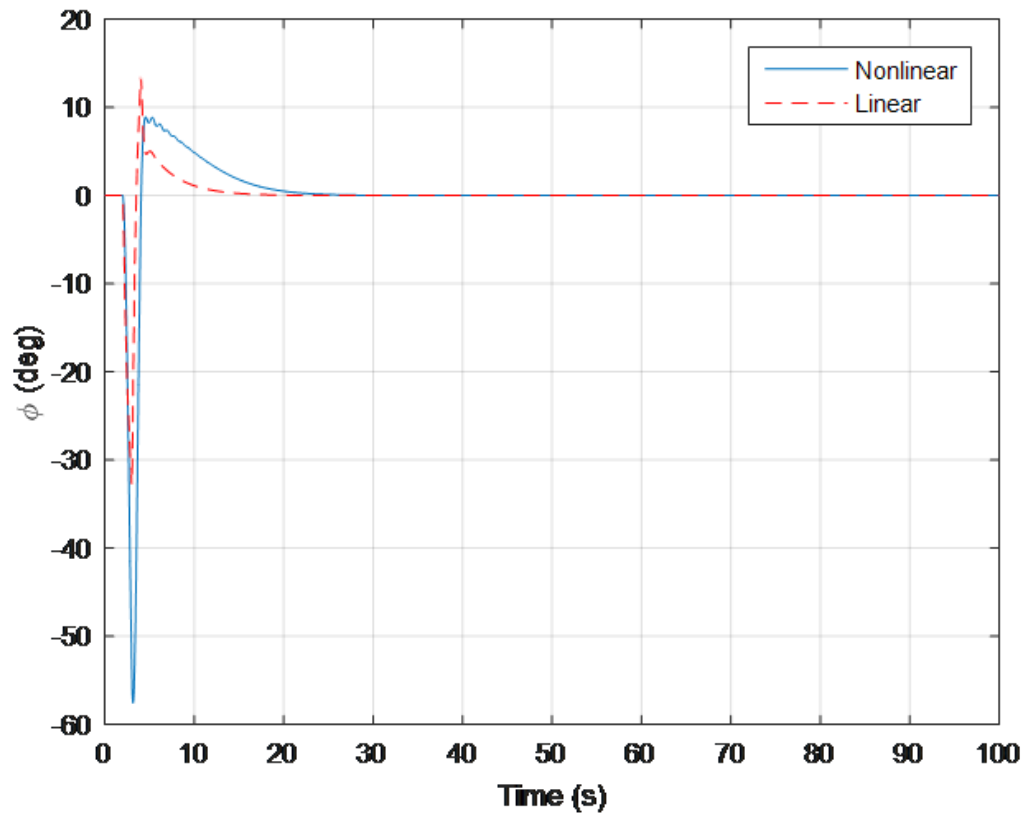


Figure 4.3. Bank Response between Linear and Nonlinear Models

while the lateral modes have the following natural frequencies, $\omega_{n,lat}$, and damping ratio, ζ_{lat}

$$\omega_{n,lat,mech} = \begin{bmatrix} 34.7689 \\ 9.0946 \\ 9.0946 \\ 0.0625 \end{bmatrix} \text{ rad/s}; \zeta_{lat,mech} = \begin{bmatrix} 1 \\ 0.2428 \\ 0.2428 \\ -1 \end{bmatrix}$$

$$\omega_{n,lat,MFC} = \begin{bmatrix} 36.1839 \\ 9.1563 \\ 9.1563 \\ 0.0182 \end{bmatrix} \text{ rad/s}; \zeta_{lat,MFC} = \begin{bmatrix} 1.0000 \\ 0.1953 \\ 0.1953 \\ 1.0000 \end{bmatrix}$$

4.1.2 Poles for the Open-Loop System

Similarly, using the linear Skywalker model in Simulink, the open-loop poles for longitudinal and lateral modes are presented in Tables 4.1 and 4.2.

Table 4.1. Poles for Longitudinal Modes of the Skywalker

Mode	Mechanical Eigenvalue	MFC Eigenvalue
Short-Period	$-16.0515 \pm 17.5993i$	$-12.6291 \pm 16.1207i$
Phugoid	$-0.2366 \pm 0.3031i$	$-0.2321 \pm 0.8732i$

Lateral Modes

Table 4.2. Poles for Lateral Modes of the Skywalker

Mode	Mechanical Eigenvalue	MFC Eigenvalue
Dutch Roll	$-2.1740 \pm 8.8298i$	$-1.7878 \pm 8.9800i$
Roll Subsidence	-34.8342	-36.1839
Spiral	-0.0564	-0.0182

4.1.3 Aircraft Dynamic Behavior through Transfer Function

Linear systems follows the principle of superposition, so the Laplace transform can be used to analyze the aircraft characteristics. These Laplace equations are obtained from the Simulink models using the `tf()` function.

The elevator-to-pitch-rate transfer function for the mechanical actuator is given by

$$\frac{q}{\delta_{e,mech}} = \frac{-291.7s^3 - 3597s^2 - 1852s - 0.1323}{s^5 + 32.55s^4 + 578.4s^3 + 281.6s^2 + 80.47s + 0.0966} \quad (4.3)$$

Whereas the elevator-to-pitch-rate transfer function for the MFC actuator is given by

$$\frac{q}{\delta_{e,MFC}} = \frac{-305s^3 - 1508s^2 - 716.4s - 0.0976}{s^5 + 25.72s^4 + 431.9s^3 + 215.3s^2 + 343.1s + 0.2696} \quad (4.4)$$

The aileron-to-bank angle transfer function for the mechanical actuator is given by

$$\frac{\phi}{\delta_{a,mech}} = \frac{-232.6s^2 - 897.7s - 17550}{s^4 + 39.12s^3 + 233.8s^2 + 2861s - 179.8} \quad (4.5)$$

and the aileron-to-bank angle transfer function for the MFC actuator is given by

$$\frac{\phi}{\delta_{a,MFC}} = \frac{-244.2s^2 - 1009s - 1.916e04}{s^4 + 39.78s^3 + 213.9s^2 + 3037s + 55.12} \quad (4.6)$$

The rudder-to-bank-angle transfer function for the mechanical actuator is given by

$$\frac{\phi}{\delta_{r,mech}} = \frac{17.94s^2 - 575.6s - 6206}{s^4 + 39.12s^3 + 233.8s^2 + 2861s - 179.8} \quad (4.7)$$

and the mechanical rudder with respect to MFC-actuated ailerons is

$$\frac{\phi}{\delta_{r,MFC}} = \frac{28.85s^2 - 250.1s - 6713}{s^4 + 39.78s^3 + 213.9s^2 + 3037s + 55.12} \quad (4.8)$$

4.2 Control Laws

There are two sections to the control laws design in this research as the Model Reference Adaptive Controller (MRAC) that is used to minimize tracking error is used in a way such that its reference model is a nonlinear aircraft model with an LQR controller. Therefore, this section will discuss about MRAC, and the LQR algorithm that is incorporated in the reference model.

4.2.1 Model Reference Adaptive Control (MRAC)

While MRAC methodologies in practical world are faced with strong resistance from practitioners and are bound to limited application, the MRAC controller is chosen for this thesis due to its agile capability to accommodate or minimizing the indeterministic disturbances coupling the usage of MFC on aircraft control surfaces.

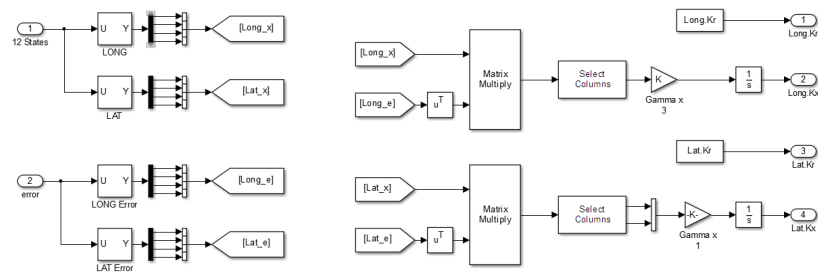


Figure 4.4. Overview of MRAC Simulated Model

The MRAC approach, as its name suggested, requires the plant to follow the behavior of a desired reference model that can be represented as

$$\dot{x}_m(t) = A_m x_m(t) + B_m u_m(t) \quad (4.9)$$

$$y_m(t) = C_m x_m(t) \quad (4.10)$$

$$x(t) \rightarrow x_m(t) \quad (4.11)$$

$$y(t) \rightarrow y_m(t) \quad (4.12)$$

with a control signal that feeds the plant in terms of linear combination of the model state variables

$$u(t) = \sum k_i x_{m_i}(t) = K x_m(t) \quad (4.13)$$

MRAC is sometimes claimed to be Pole-Zero placing as the entire plant state ultimately converges to behave exactly like the model state (Wen & Balas, Wen & BalasWen & Balas1989).

Unknown plant parameters due to the use of MFC ailerons are taken into account with the use of adaptive control gains. The main idea is to feed a control signal, which is a linear combination of the model state, to the plant through chosen gains. Accurate gains will result in perfect tracking of the plant with respect to its model reference. However, inaccurate gain values, mainly due to uncertainties in the plant, will more than likely result in a output tracking error given in the form of

$$e_y(t) = y_m(t) - y(t) \quad (4.14)$$

This error is monitored and used to generate adaptive gains

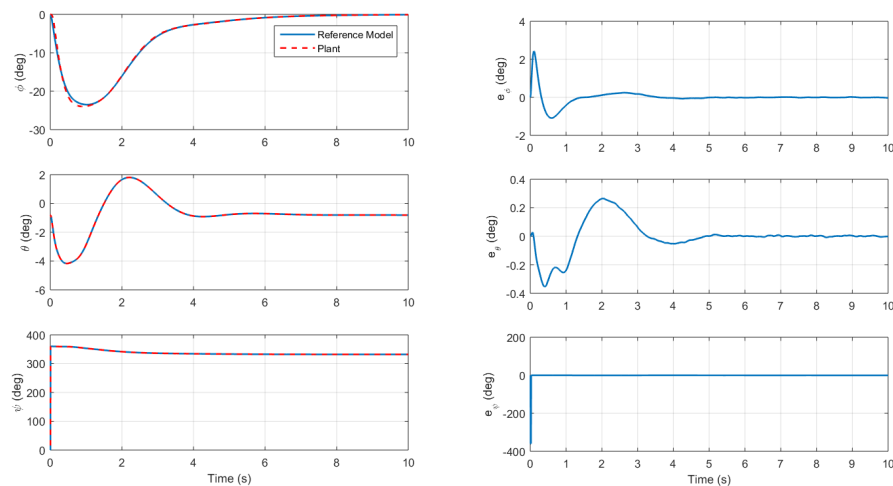
$$\dot{K}_x(t) = \Sigma \gamma_i e_y(t) x_{mi}(t) = e_y(t) x_m^T(t) \Gamma_x \quad (4.15)$$

$$u(t) = \Sigma k_{xi}(t) = K_x(t) x_m(t) \quad (4.16)$$

where γ_i affects the rate of adaptation. The adaptation continues until the correlation error between the tracking output and state variable diminishes, resulting in a zero gain derivative that gives us a constant gain value. This method showed that the entire state error

$$e_x(t) = x_m(t) - x(t) \quad (4.17)$$

asymptotically vanishes, as shown in Figures 4.5 and 4.6:



(a) Systems Output

(b) Tracking Error

Figure 4.5. Systems Output and Error Tracking of Regular Plant

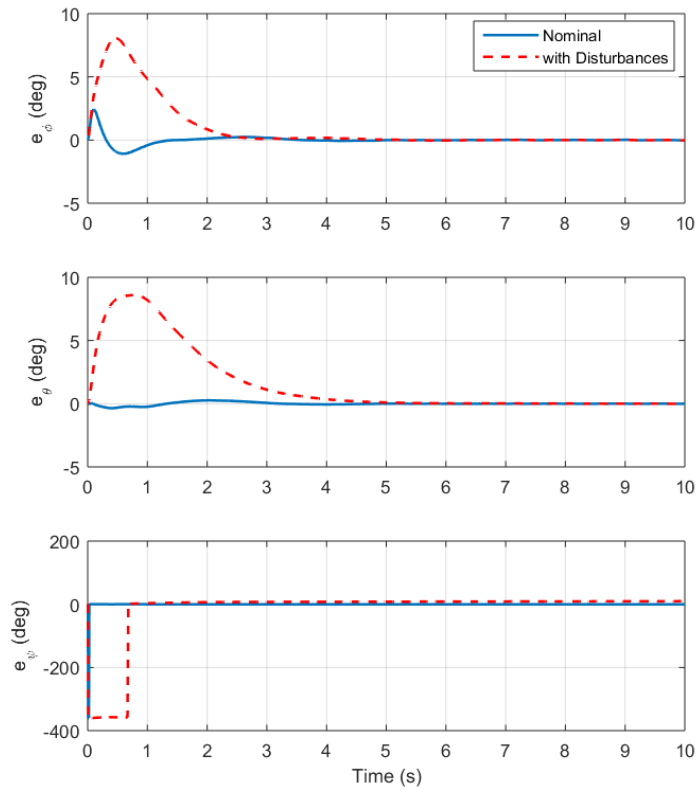


Figure 4.6. Tracking Error Comparison Between Nominal and Disturbed Flights

The results imply that the plant behavior asymptotically reproduced the behaviors of the reference model and ultimately achieved its desired performance represented by the reference. These graphs are plotted during a random trajectory-tracking flights to show case that the actual plant behaves similar to the reference model, and that the reference-tracking errors are diminished with time. The disturbances that was added to plot the output tracking error graphs in Figure 4.6 are injected in the form of additional control surfaces deflection that are fed into the actual plant.

4.3 Linear Quadratic Regulator (LQR)

As the name MRAC suggested, there is a reference model that is used to guide the behaviors of the simulated plant. This model is a twin copy of the plant with an additional LQR controller.

The simulated plant is described by

$$\begin{aligned}\dot{x} &= Ax + Bu \\ y &= Cx\end{aligned}\tag{4.18}$$

with state $x(t)$, control input $u(t)$, and $y(t)$ as the measured output available for feedback purposes. Aside from those variables, the performance output $z(t)$ that is not usually equal to $y(t)$ is defined as

$$z = Hx\tag{4.19}$$

The dynamic compensator has the form

$$\begin{aligned}\dot{w} &= Fw + Ge \\ v &= Dw + Je\end{aligned}\tag{4.20}$$

with state $w(t)$, output $v(t)$, and input equal to the tracking error

$$e(t) = r(t) - z(t)\tag{4.21}$$

The allowed form for the plant control is

$$u = -Ky - Lv\tag{4.22}$$

where the constant gains K and L are chosen to output satisfactory $r(t)$. This formulation allows for feedback and feedforward compensator dynamics.

These equations can be written in augmented form as

$$\begin{bmatrix} \dot{x} \\ \dot{w} \end{bmatrix} = \begin{bmatrix} A & 0 \\ -GH & F \end{bmatrix} \begin{bmatrix} x \\ w \end{bmatrix} + \begin{bmatrix} B \\ 0 \end{bmatrix} u + \begin{bmatrix} 0 \\ G \end{bmatrix} r \quad (4.23)$$

$$\begin{bmatrix} y \\ v \end{bmatrix} = \begin{bmatrix} C & 0 \\ -JH & D \end{bmatrix} \begin{bmatrix} x \\ w \end{bmatrix} + \begin{bmatrix} 0 \\ J \end{bmatrix} r \quad (4.24)$$

$$z = \begin{bmatrix} H & 0 \end{bmatrix} \begin{bmatrix} y \\ w \end{bmatrix} \quad (4.25)$$

By redefining the state, the output, and the matrix variables to streamline the notation, the augmented equations that contain the dynamics of the aircraft and the compensator are in the form of

$$\dot{x} = Ax + Bu + Gr \quad (4.26)$$

$$y = Cx + Fr \quad (4.27)$$

$$z = Hx \quad (4.28)$$

where state $x(t) \in \mathbf{R}^n$, control input $u(t) \in \mathbf{R}^m$, reference input $r(t) \in \mathbf{R}^q$, performance output $z(t) \in \mathbf{R}^q$, and measured output $y(t) \in \mathbf{R}^p$. The permissible controls are proportional output feedbacks of the form

$$u = -Ky = -KCx - KFr \quad (4.29)$$

with constant gain, K . Using these equations, the closed-loop system is

$$\begin{aligned}\dot{x} &= (A - BKC)x + (G - BKF)r \\ &\equiv A_c x + B_c r\end{aligned}\tag{4.30}$$

$$\begin{bmatrix} \dot{x} \\ \dot{w} \end{bmatrix} = \begin{bmatrix} A & 0 \\ -C & 0 \end{bmatrix} \begin{bmatrix} x \\ w \end{bmatrix} + \begin{bmatrix} B \\ 0 \end{bmatrix} u + \begin{bmatrix} 0 \\ 1 \end{bmatrix} r(t)$$

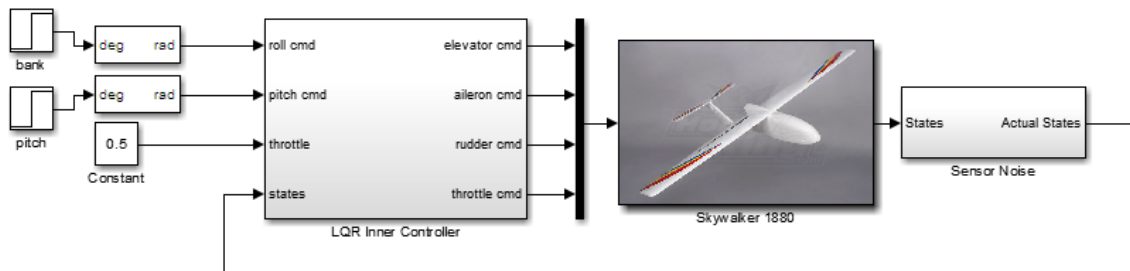


Figure 4.7. Outer Loop Controller using LQR

Figure 4.8 shows the results of tracking the desired pitch and roll commands.

4.4 Waypoint Navigation

The waypoint navigation calculated is conducted by simply comparing the difference between the relative bearing of the airplane position and its next waypoint.

The relative bearing is calculated using

$$\psi_{rel}(k) = \rho(k) - \psi_{GPS}(k)\tag{4.31}$$

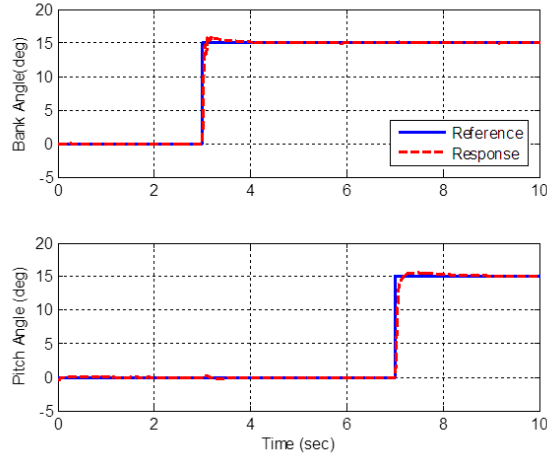


Figure 4.8. Controller Response to Commands

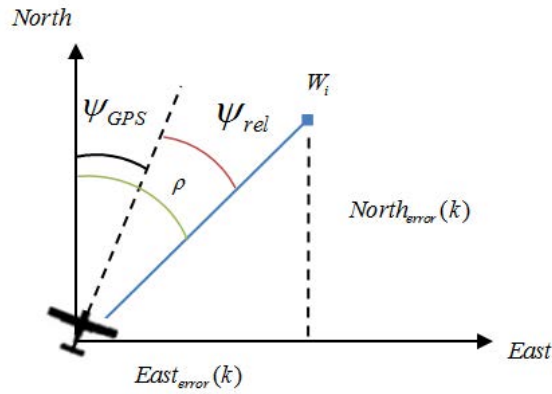


Figure 4.9. Bearing Calculation Derivation for Waypoint Navigation

where ψ_{GPS} is the course heading from the GPS. The bearing to the station is calculated as

$$\rho(k) = \arctan2\left(\frac{East_{error}(k)}{North_{error}(k)}\right) \quad (4.32)$$

Instead, the earth error is used as the current position of the aircraft in the NED frame relative to the desired waypoint, W_i , which is updated to the next waypoint, W_{i+1} in the list once the airplane reaches within a user-specified radial range of

the waypoint. The last range-to-target and bearing-to-station, due to the lack of subsequent waypoint, is calculated as follow.

The range to the target is

$$a = \sin^2\left(\frac{\Delta\psi}{2}\right) + \cos(\psi_1) \cdot \cos(\psi_2) \sin^2\left(\frac{\Delta\lambda}{2}\right) \quad (4.33)$$

$$c = 2 \cdot \text{atan2}(\sqrt{a}, \sqrt{1-a}) \quad (4.34)$$

$$d = R \cdot c \quad (4.35)$$

The bearing to the station is calculated using

$$\rho(k) = \text{atan2}(\sin(\Delta\lambda) \cdot \cos(\psi_2), \cos(\psi_1) \cdot \sin(\psi_2) - \cos(\psi_2) \cdot \sin(\psi_1) \cdot \cos(\Delta\lambda)) \quad (4.36)$$

where ψ_1 represents current latitude, ψ_2 represents target latitude, λ_1 represents current longitude, λ_2 represents target longitude, and R is the radius of Earth.

As an example, Figure 4.10 shows that the UAV with mechanical actuator correctly following the desired waypoints at a constant altitude.

However, with the reduced aileron size, lift coefficient, and deflection angle, the UAV with MFC actuator, while is capable of maintaining altitude, struggles to accurately track the desired waypoints. The best outcome obtained from tuning the LQR+i controller yields an actual trajectory that resembles the shape of the desired trajectory with huge deviation in precision.

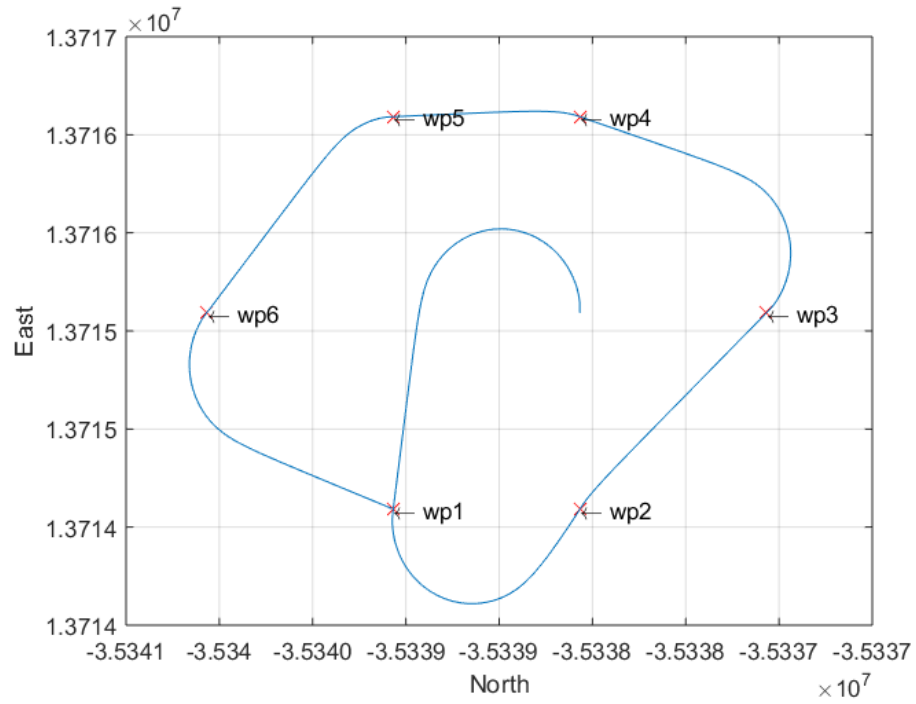


Figure 4.10. Waypoint Navigation Logic Implementation with Mechanical Actuator

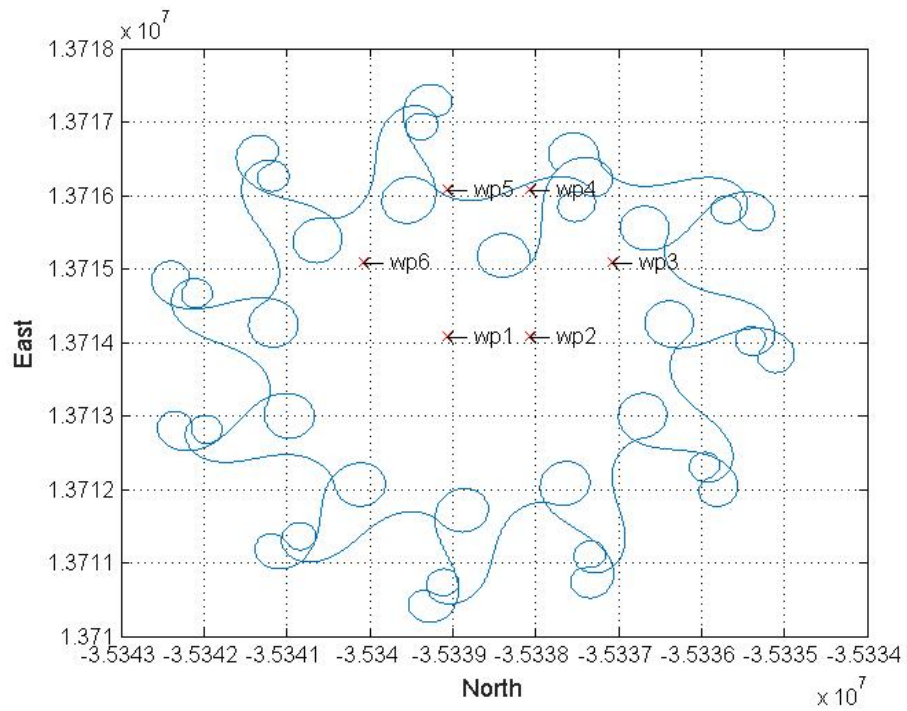


Figure 4.11. Waypoint Navigation Logic Implementation with MFC Actuator

5. Performance Evaluation

To demonstrate the functionality of the actuator models, a series of simulation tests were performed for mechanical and MFC-actuated ailerons at nominal and abnormal flight conditions. For the abnormal flight condition, disturbances are injected to the control surfaces in the form of additional deflection angles. All simulation tests are performed at a certain point within the same flight envelope at a cruising speed of 70ft/s and an altitude of 200ft. Among the flight paths considered for this analysis are the Oval and Figure-8, as shown in Figure 5.1.

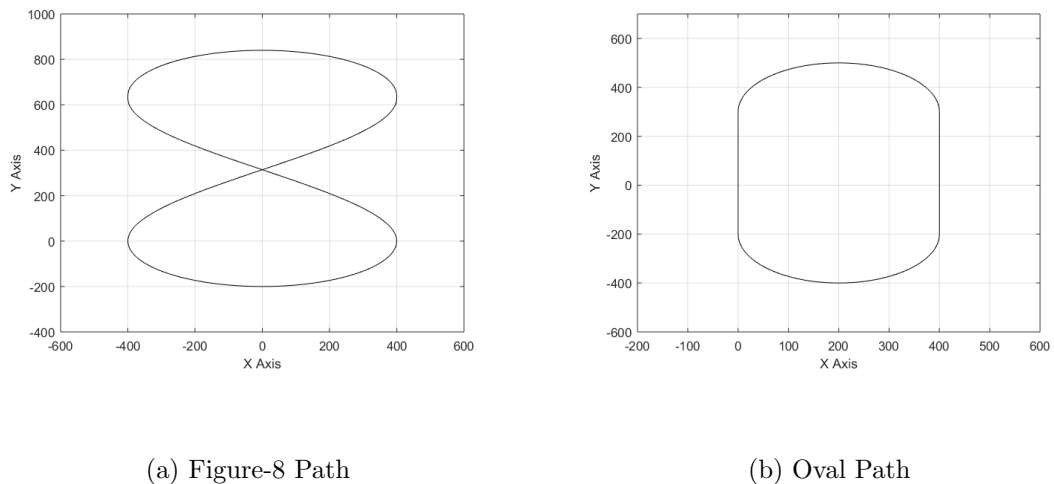


Figure 5.1. Navigation Flight Path

Each trajectory-tracking algorithm is used to track the aircraft performance at nominal condition using mechanical and MFC-actuated ailerons, as well as abnormal condition consisting of excessive turbulence.

5.1 Performance Metrics

Few metrics exist for positional or trajectory tracking evaluation. To name a few, there are comparison of trajectories, spatially separated trajectories, temporally separated trajectories, spatio-temporally separated trajectories, and area between trajectories (Needham & Boyle, Needham & BoyleNeedham & Boyle2003). The comparison of trajectories method is used in this research.

The performance of each flight is measured based on its trajectory tracking error and control activity. Consider two trajectories composed of two-dimensional positions at a sequence of time steps, the difference between positions at a specific time step is known as the error terms. These error terms, in this case, are defined as the horizontal-plane trajectory tracking error, $e_h(t)$, and vertical trajectory tracking error, $e_z(t)$ (Moncayo, Perhinschi, Wilburn, Wilburn, & Karas, Moncayo, Perhinschi, Wilburn, Wilburn, & KarasMoncayo et al.2012).

$$e_h(t) = \sqrt{[x_c(t) - x(t)]^2 + [y_c(t) - y(t)]^2} \quad (5.1)$$

$$e_z(t) = |z_c(t) - z(t)| \quad (5.2)$$

These two terms combine to provide an overall XYZ tracking error term, $e_{XYZ}(t)$, that represents the distances between positions at given time.

$$e_{XYZ}(t) = \sqrt{[x_c(t) - x(t)]^2 + [y_c(t) - y(t)]^2 + [z_c(t) - z(t)]^2} \quad (5.3)$$

All of the trajectory tracking related evaluation parameters are divided into three main categories that calculate the average, maximum, and standard deviation of the error values obtained from each plane. These parameters are listed as the followings:

The average horizontal-plane trajectory tracking error is

$$\bar{e}_{XY} = \text{mean}(|e_{XY}(t)|) \quad (5.4)$$

The average vertical trajectory tracking error is

$$\bar{e}_Z = \text{mean}(|e_Z(t)|) \quad (5.5)$$

The average combined XYZ trajectory tracking error is

$$\bar{e}_{XYZ} = \text{mean}(|e_{XYZ}(t)|) \quad (5.6)$$

The maximum horizontal-plane trajectory tracking error is

$$\bar{e}_{max,XY} = \text{max}(|e_{XY}(t)|) \quad (5.7)$$

The maximum vertical trajectory tracking error is

$$\bar{e}_{max,Z} = \text{max}(|e_Z(t)|) \quad (5.8)$$

The maximum combined XYZ trajectory tracking error is

$$\bar{e}_{max,XYZ} = \text{max}(|e_{XYZ}(t)|) \quad (5.9)$$

The standard deviation of the horizontal-plane trajectory tracking error is

$$\hat{e}_{XY} = std(e_{XY}(t)) \quad (5.10)$$

The standard deviation of the vertical trajectory tracking error is

$$\hat{e}_Z = std(e_Z(t)) \quad (5.11)$$

The standard deviation of the combined XYZ trajectory tracking error is

$$\hat{e}_{XYZ} = std(e_{XYZ}(t)) \quad (5.12)$$

The trajectory tracking (TT) specific performance vector is then defined as

$$PV_{TT} = [\bar{e}_{XY} \quad \bar{e}_Z \quad \bar{e}_{XYZ} \quad e_{max,XY} \quad e_{max,Z} \quad e_{max,XYZ} \quad \hat{e}_{XY} \quad \hat{e}_Z \quad \hat{e}_{XYZ}]^T \quad (5.13)$$

It is crucial that the TT algorithm supplies gradual commands that do not saturate the deflection of the control surfaces. Hence, the evaluation is done based on the rate of change in deflection and the saturation index for each control surfaces. The controls activity related evaluation parameters are defined as the followings:

The integral of control command or the rate of change of control surfaces deflection is

$$I\dot{\delta}_c = \frac{1}{T} \int_0^T |\dot{\delta}_c| dt \quad (5.14)$$

The control command or deflection saturation index

$$S_{\delta_c} = \frac{100}{T} \int_0^T \tilde{\delta}_c(t) dt \quad (5.15)$$

with

$$\tilde{\delta}_c(t) = \begin{cases} 0, & \delta_c < \delta_{c,max} \\ 1, & \delta_c > \delta_{c,max} \end{cases} \quad (5.16)$$

where δ_c represents the control command or control surface deflection and T represents the total simulation time. In this case, the control surfaces and command involved are the elevator δ_e , the ailerons δ_a , the rudder δ_r , and throttle δ_T (Moncayo et al., Moncayo, Perhinschi, Wilburn, Wilburn, & KarasMoncayo et al.2012).

Control activity specific performance vector is defined as:

$$PV_{CA} = [I\dot{\delta}_e \quad I\dot{\delta}_a \quad I\dot{\delta}_r \quad I\dot{\delta}_T \quad S_{\delta_e} \quad S_{\delta_a} \quad S_{\delta_r} \quad S_{\delta_T}]^T \quad (5.17)$$

In order to strip the large group of data down to a meaningful representation, performance indices are formulated for each tracking algorithm, based on weighted sum of the normalized components within each performance parameters.

Trajectory tracking specific performance index can be defined as

$$PI_{TT} = w_{TT} \cdot PV_{TT} \quad (5.18)$$

whereas control activity specific performance index can be defined as

$$PI_{CA} = w_{CA} \cdot PV_{CA} \quad (5.19)$$

These two indices sum up to form a trajectory tracking global performance index as defined below.

$$PI_{UAV} = \bar{w}_{TT} \cdot PI_{TT} + \bar{w}_{CA} \cdot PI_{CA} \quad (5.20)$$

where w_{TT} , w_{CA} , \bar{w}_{TT} , and \bar{w}_{CA} are weight normalization and desirability.

Table 5.1. Performance Index Weight and Normalization Cut-off Values for Trajectory Tracking

	Mean			Max			Std. Deviation		
	XY	Z	XYZ	XY	Z	XYZ	XY	Z	XYZ
Normalization Cut-off	50	50	50	10	10	10	5	5	5
w_{TT}	0.06	0.08	0.06	0.12	0.16	0.12	0.12	0.16	0.12
\bar{w}_{TT}	0.5								

5.2 Actuator Performance Analysis

The nominal and abnormal flight condition performance of the MFC-actuated ailerons is compared with the performance of the original mechanically-actuated ailerons. Four different trajectories that requires varying maneuvers are used to evaluate controller performance. For each of these trajectories, nominal flight and flight with disturbances, injected in the form of additional control surfaces deflection, are applied to both of the mechanical and MFC ailerons. The disturbances are injected in the form of amplified control surfaces movement. The collected data are normalized and their performance indices are computed using the normalization cut-off values and desirability weights listed in the Tables 5.1 and 5.2.

Figures 5.1 and 5.2 consist of the trajectory tracking and control activity errors of the mechanical and MFC-actuated ailerons. The nominal flight condition with MFC-actuated ailerons show an average XYZ trajectory error of about 230ft, maximum XYZ error of approximately 517ft, as well as, a standard deviation XYZ error of

Table 5.2. Performance Index Weight and Normalization Cut-off Values for Control Activity

	Surface Activation Index				Saturation Index			
	δ_e	δ_a	δ_r	δ_T	δ_e	δ_a	δ_r	δ_T
Normalization Cut-off	0.5	0.5	0.5	20	100	100	100	100
w_{CA}	0.1	0.1	0.1	0.2	0.1	0.1	0.1	0.2
\bar{w}_{CA}	0.5							

about 140ft. When compared to the error values of the mechanical ailerons that are all within 10ft, the MFC-actuated aileron configuration values are a poor deflection of its performance.

Flight Condition	Actuator	Mean			Max			Standard Deviation		
		XY	Z	XYZ	XY	Z	XYZ	XY	Z	XYZ
		[ft]	[ft]	[ft]	[ft]	[ft]	[ft]	[ft]	[ft]	[ft]
Nominal	Mechanical	0.000	6.978	6.978	0.000	22.407	22.407	0.000	7.387	7.387
	MFC	229.446	0.000	229.446	516.697	0.000	516.697	138.372	0.000	138.372
With Disturbance	Mechanical	0.000	67.077	67.077	0.000	219.748	219.748	0.000	66.762	66.762
	MFC	739.058	0.000	739.058	1219.090	0.000	1219.090	428.680	0.000	428.680

Figure 5.2. Trajectory Tracking

Flight Condition	Actuator	Integral of Control Surface Rate of Change				Saturation Index			
		Elevator	Aileron	Rudder	Throttle	Elevator	Aileron	Rudder	Throttle
		[rad/s]	[rad/s]	[rad/s]	[%]	[%]	[%]	[%]	[%]
Nominal	Mechanical	0.0011	0.0353	0.0034	7.63	0	0	0	0
	MFC	0.0119	0.0258	0.0063	8.76	0	6.32	23.54	0
With Disturbance	Mechanical	0.0282	0.0378	0.0123	7.63	0	0	0	0
	MFC	0.0111	0.0867	0.0051	8.76	0	27.18	27.34	0

Figure 5.3. Control Activity

The following is a summary of the performance details for Oval and Figure-8 trajectory for mechanical and MFC-actuated ailerons. While the mechanical setup has a PI_{TT} of 0.724 for the Oval path and 0.7555 for the Figure-8 path, the MFC configuration shows PI_{TT} of zero for both of the given paths. This outcome indicates that the UAV with the MFC-actuated ailerons is unable to complete the given tasks. For the oval path mission, the MFC actuator control activity's performance index exceeds that of the mechanical actuator, which shows that it requires less actuation to track the trajectory compared to the mechanical ailerons.

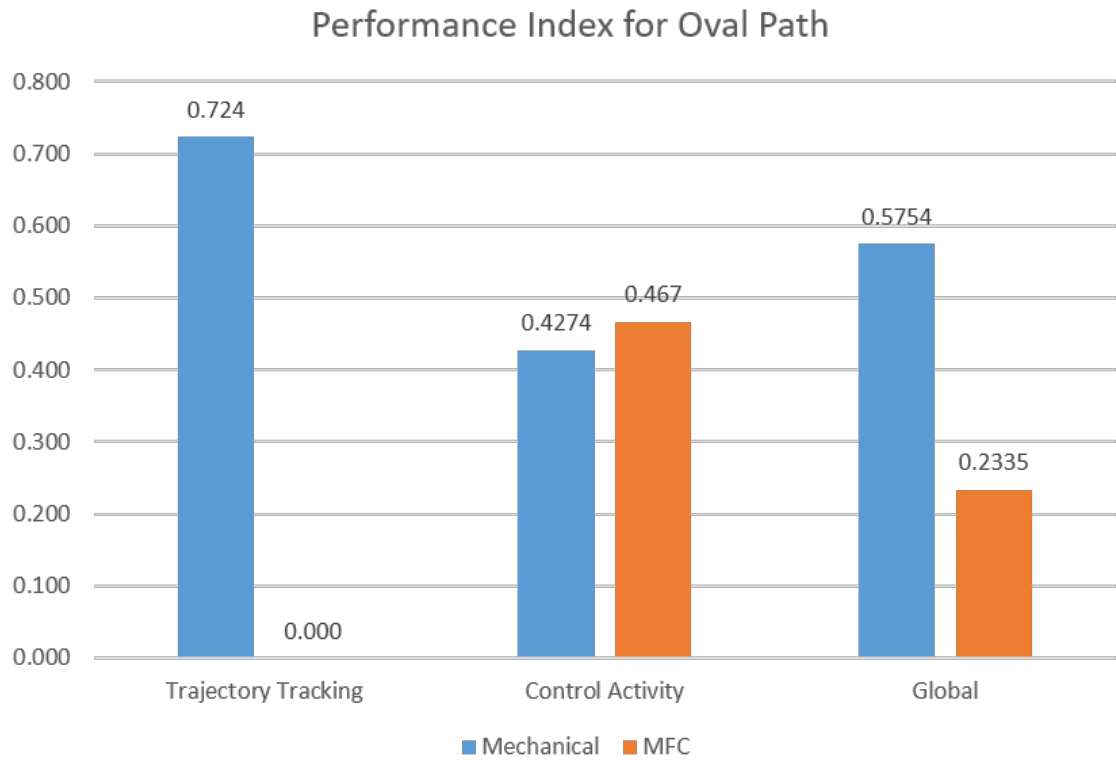


Figure 5.4. Performance Index Summary for Oval Path

The results show that the mechanical-actuated ailerons exhibit a more desirable performance than the MFC-actuated ailerons. To further confirm the outcome based on performance index, Figure 5.4 illustrates a failed attempt at tracking an oval path using the MFC-actuated ailerons.

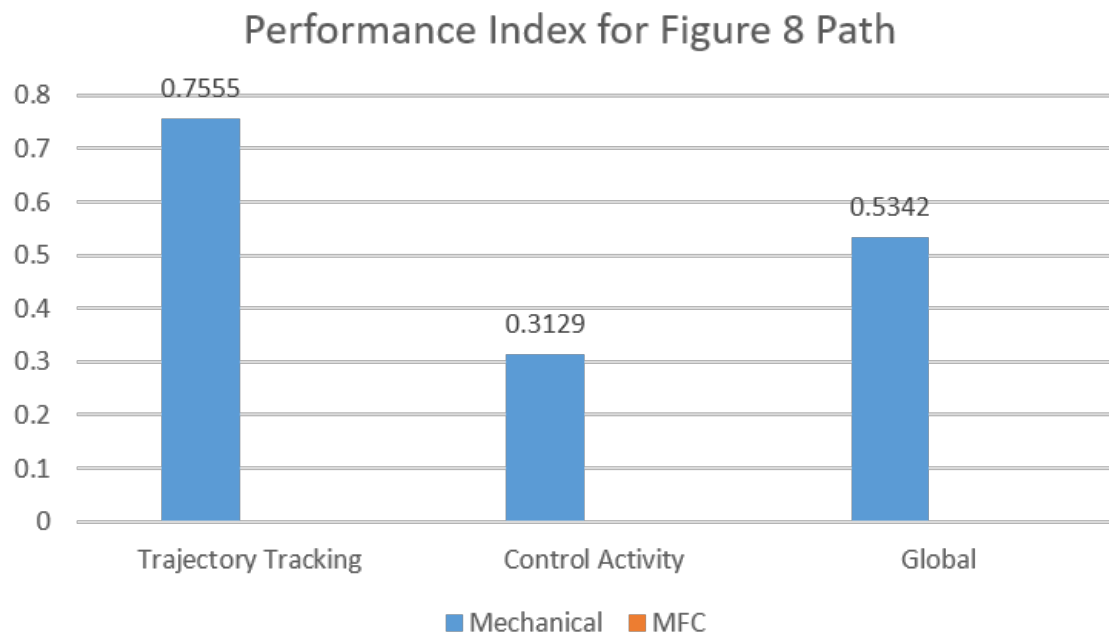


Figure 5.5. Performance Index Summary for Figure-8 Path

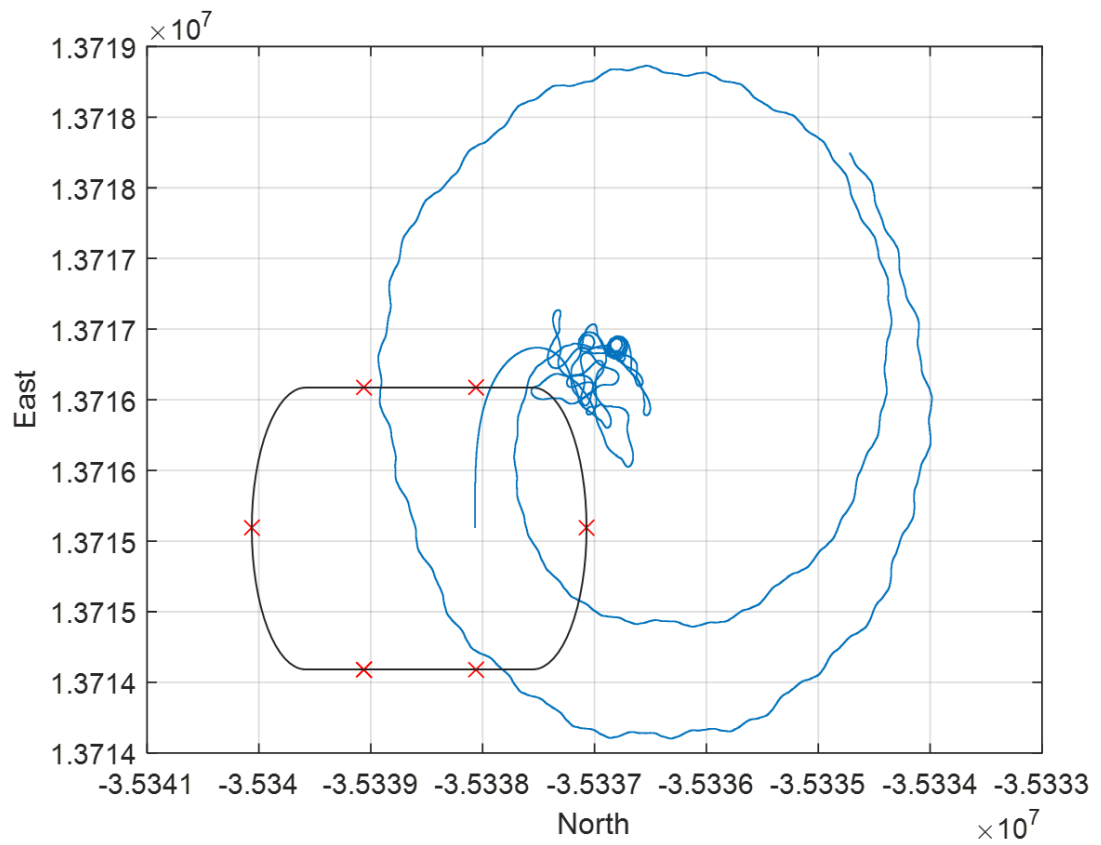


Figure 5.6. Trajectory Tracking for Oval Path Using MFC-Actuated Ailerons

6. System Integration for Future Development

As mentioned earlier in the simulation environment section of this thesis, the "New Skywalker 1880" was chosen as the test platform for the MFC ailerons. The choice was made with the basis to offer a stable and affordable system that satisfies the requirements for flight tests. With a stronger and denser built compared to its predecessors, the wings are interchangeable with wings from other models and the aircraft also comes with a carbon fiber tail that offers a stronger and lighter structure for better flight performance.



Figure 6.1. Skywalker 1880 Assembled RC Model with MFC Halved-Ailerons

6.1 Hardware Integration

The Skywalker 1880 is fitted with analog and digital sensors for flight test and data collection purposes. The heartbeat of the entire on-board setup that outputs commands and collects flight data is a micro-controller with an Atmel ATMEGA 2560 processor assembled into the Ardupilot Mega (APM) 2.6. An overview of the hardware integration circuit is presented in Figure 6.2.

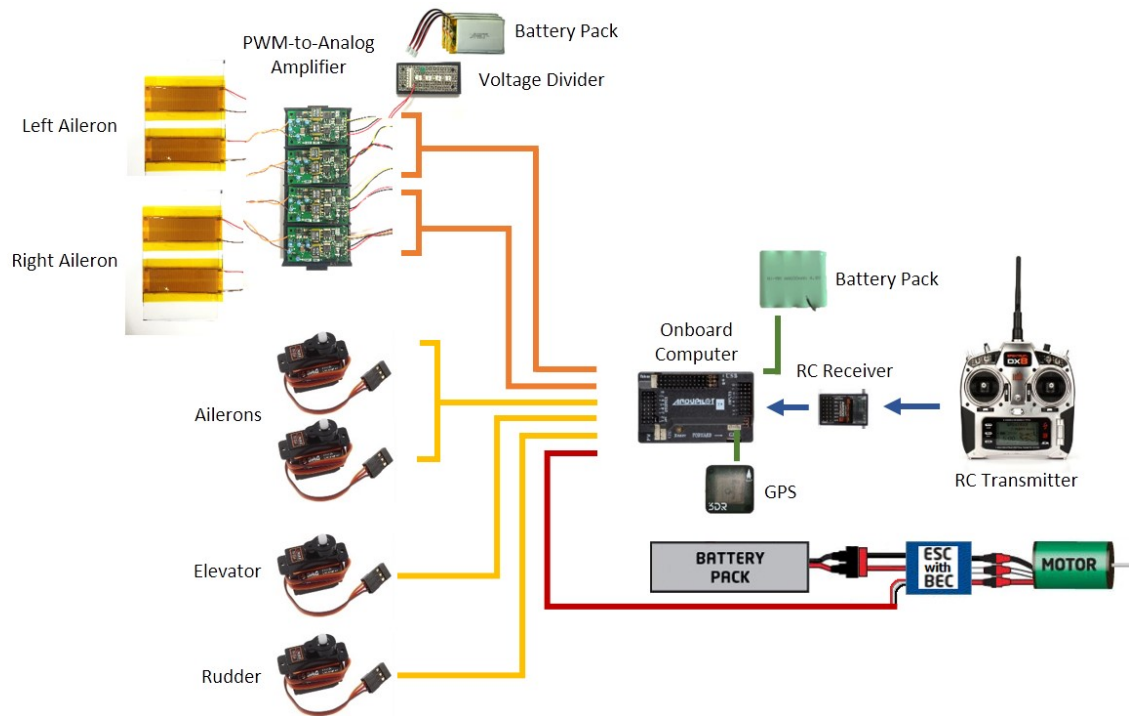


Figure 6.2. Overview of Hardware Integration in the Skywalker 1880

6.1.1 Instrumentation

APM 2.6

The APM 2.6 that is used for this mission is an open source autopilot solution produced by 3D Robotics. With the casing, it weighs about 0.71oz with a dimension of 2.9x1.6in. The APM 2.6 utilizes an 8-bit, 16 MHz Atmel AT Mega 2560 processor that comes with 54 digital I/O pins in which 14 of them can be used for PWM signals. Also included in this system is a data flash card that has a capacity of 4Mb and the capability to record up to 17 minutes of 20 floating point parameters at 50Hz.

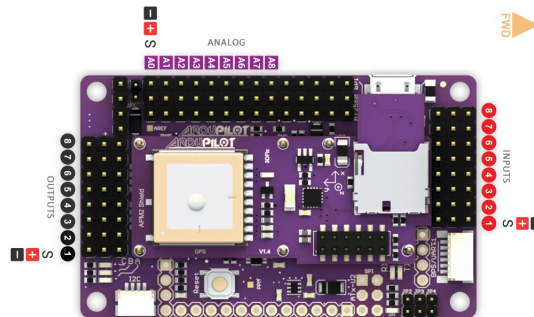


Figure 6.3. APM 2.6 Overview

InvenSense MPU-6000 Inertial Sensor

The MPU-6000 is a 6-axes motion tracking device that combines a 3-axes gyroscope and a 3-axes accelerometer in a 0.15x0.15x0.035in QFN footprint.



Figure 6.4. InvenSense MPU-6000

MediaTek MT3329 GPS

With a dimension of 1.5x0.6x0.3in and weighs only 0.3oz, the MT3329 is a 66-channel single chip solution with a binary output protocol that updates up to a 10Hz rate. It has tracking capability with a sensitivity up to -165dB and a position accuracy of less than 10ft. It comes with USB/UART interfaces for data transfer purpose.



Figure 6.5. MediaTek MT3329

MEAS Switzerland MS5611 Barometric Pressure Sensor

This barometric pressure sensor consists of a high resolution altimeter sensor with SPI and I2C bus interfaces up to 20MHz in a 0.2x0.1x0.04in QFN footprint. Its factory calibrated sensor has a resolution of 3.9in.



Figure 6.6. MS5611-01BA093 Barometric Pressure Sensor

Free-scale MPXV7002DP Differential Pressure Sensor

This analog sensor has maximum rating for pressure up to 2kPa at 60deg C . It is directly attached to a miniature pitot-tube that is located on the right wing of the airplane to capture true airspeed measurements that are required for the control laws.



Figure 6.7. Pitot Tube and Pressure Sensor

XBee Transceiver

The XBee XSC with SMA antenna can operate in two modes: transparent data mode or packet-based application programming interface (API) mode. The API mode

allows the team to address and set parameters as well as packet delivery feedback, including remote sensing and control of digital I/O and analog input pins.



Figure 6.8. XBee Transceiver Module

Spektrum DX8 Transmitter and Receiver

The Spektrum DX8 transmitter and receiver are used for manual control of the aircraft and the switching between mechanical and MFC ailerons setup. It is equipped with 8-channel radios, up to 2.4GHz, with Intuitive Simple ScrollTM Interface for navigation purpose. Four channels are used for the control of rudder, elevator, mechanical ailerons, and throttle; 2 channels are dedicated to the control of the MFC ailerons; and the seventh channel is used as a switch command between aileron setups. In total, the transmitter allows for adjustments up to 9 types of wing setting, 5 types of tail setting, and 6 programmable flight maneuver mixes.



Figure 6.9. Spektrum DX8 Transmitter and Receiver

Turnigy D3542/6 Brushless Motor

The Turnigy D3542/6 chosen for the Skywalker 1880 is a 1000Kv RPM brushless motor with a maximum current draw of 38A and provides a maximum power of 665W. It weighs about 0.3lb, with a dimension of 1.38x1.65in and a 0.2in shaft diameter.



Figure 6.10. Turnigy Brushless Motor

Turnigy 5000mAh Lipo Battery

Three voltage values are used for our aircraft to power the autopilot system, the MFC ailerons, and its propeller. A 4.8V battery is used to power the RC receiver, the APM 2.6 board, and the sensors onboard of the aircraft during flight, while the amplifiers connected to the MFC ailerons are powered by a 10.8V battery and the propellers are powered by 14.8V battery pack.



Figure 6.11. Turnigy 5000mAh Lipo Battery

6.1.2 AMT2012-CE3 Dual High Voltage Amplifier

The AMT2012-CE3 is a triple output power supply with one fixed 500V bias supply and two variable outputs ranging from 0 to 2kV. This amplifier is specifically design for the MFC and supplies the a voltage range between -500 to 1500V, using PWM signals as control inputs. It has a dimension of 2.2x1.8x0.75in.

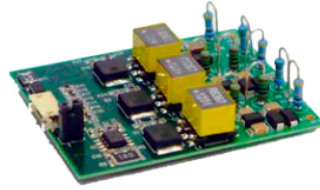


Figure 6.12. AMT2012-CE3 Amplifier

6.2 Software Integration

6.2.1 Simulink Models

The APM2 Block set in the Simulink library made targeting the onboard microcontroller more user-friendly through model-based interface. This feature provides a great advantage for any effort involving low cost autopilots and sensor fusions boards. A simulink architecture including the reference model, adaptive controller, and Extended Kalman filter integrated with the sensor blocks from the APM2 library were designed and loaded into the APM2.6 for flight test purpose. The model showed in the figure below allows data logging of on-board sensors reading. The recorded data can be downloaded from the flash memory and analyzed after flight tests.

APM Sensors

Simulink's capability to support low-cost embedded hardware through the built-in "Run on Target Hardware" function allows automatic code generation of the targeted hardware, in this case the APM2.6, using Simulink blocks. The APM 2.0 Simulink blockset that was designed by previous Embry-Riddle students simplified the process

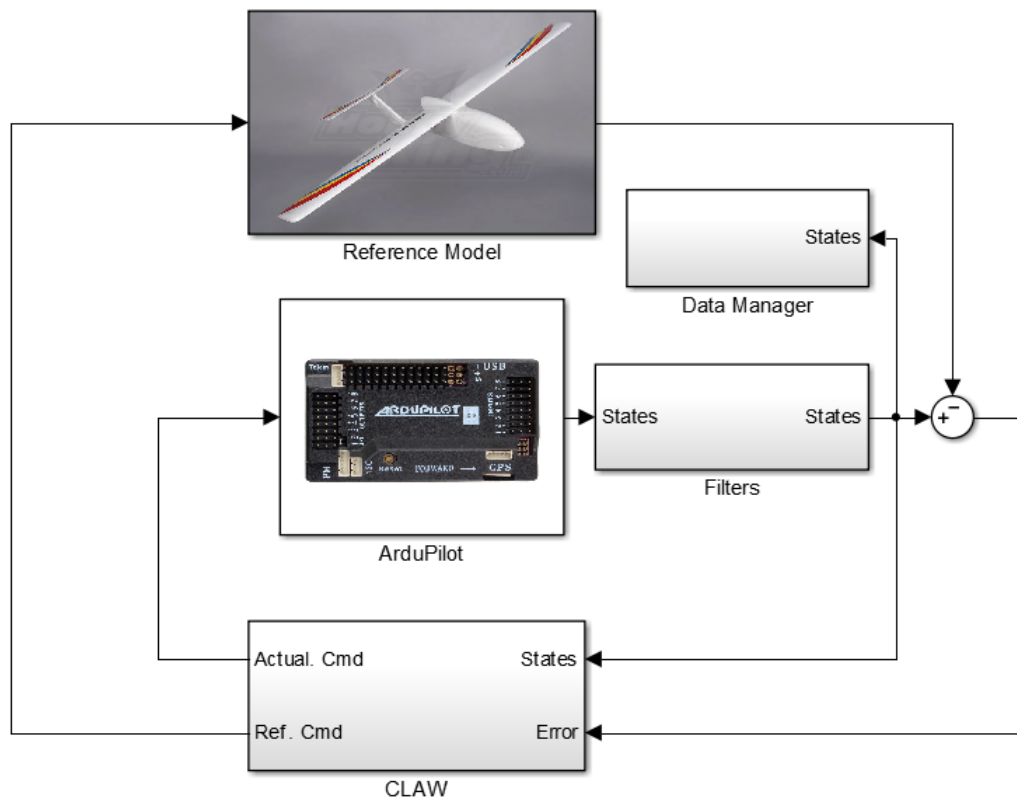


Figure 6.13. Overview of APM-integrated Simulink Model

of programming the arduino board, allowing users to read data from the embedded sensors in the Skywalker and to output control commands to the servos in the form of PWM signals. The library is featured below.

A Simulink subsystem is designed with the sole purpose to read, convert, and save data to flash memory using the sensor blocks provided by the APM 2.0 library. The figures below show the data-logging subsystem and the sensor blocks that are included in the Sensor Block module.

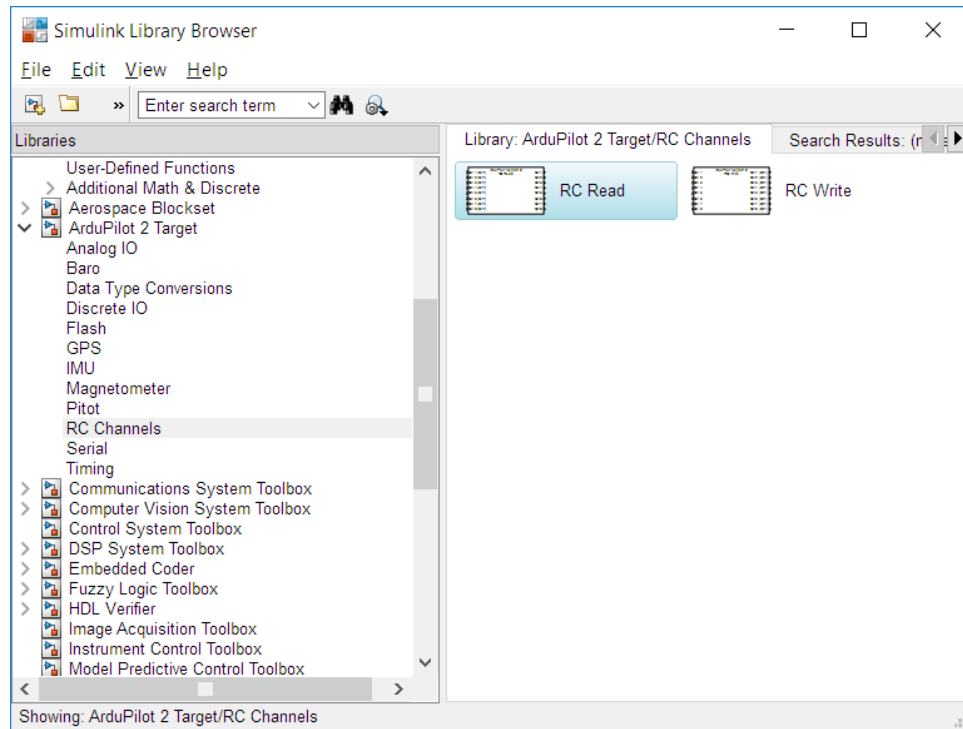


Figure 6.14. APM 2.0 Blockset in the Simulink Library

Filters Algorithm

6.2.2 Signal Conversion

The use of bimorph configuration in the MFC ailerons urged the need to design a Simulink logic for signal conversion during flights. As the ailerons only deflect in the upwards direction and has a minimum deflection of 0deg, the PWM signals that is transmitted from the radio-controlled transmitter need to be fitted in such a way to ensure maximum deflection of the MFC in one direction during flight, instead of using its default setting that includes upwards and downwards aileron deflections. The designed logic is illustrated in Figure 6.17.

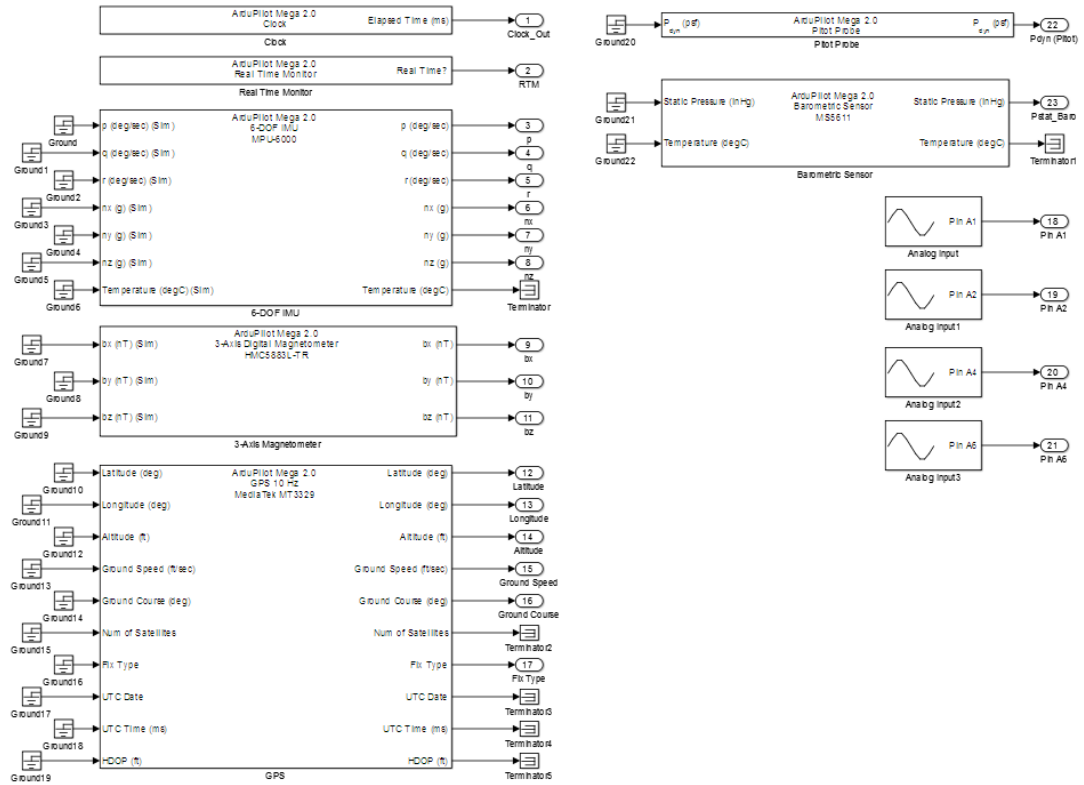


Figure 6.15. Simulink Sensor Model

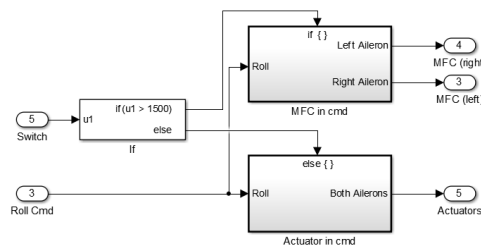


Figure 6.16. Switch Command between Mechanical and MFC Ailerons

To obtain the values used in the designed logic, the APM was connected to the amplifier in external mode and the voltage output from the amplifier was measured with respect to the PWM signals output from the APM. As observed from Figure 6.18, a neutral MFC actuator position with zero deflection requires PWM values between 1100 and 1260, while the original neutral position for ailerons with PWM signals input requires a PWM value around 1500. A logic was implemented to maintain both of the MFC actuators at their neutral position at PWM values between 1450 and 1550, at the same time, to have an upwards deflection on the right aileron while the left aileron remains at its neutral position during a positive roll, and vice versa. With all these setup, the Skywalker was ready for the flight test.

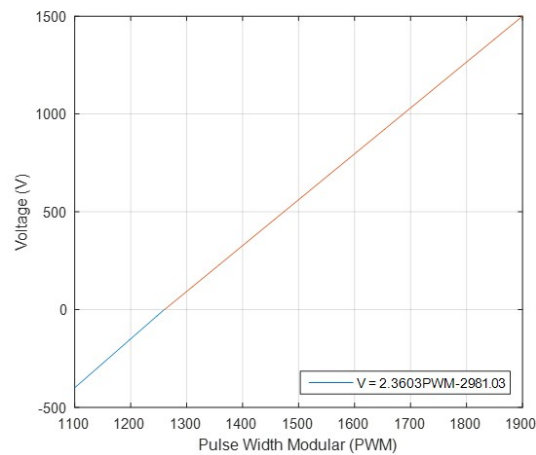


Figure 6.17. PWM-to-Voltage Conversion

7. Conclusion and Recommendation

In this paper, simulation testing of the mechanical and MFC-actuated ailerons at nominal and abnormal flight conditions were presented. While the wind tunnel testing showed promising results for the lift and drag coefficients of the wing, the simulation and flight test results have proven otherwise. Two flight tests were attempted for the MFC-actuated ailerons configuration but met with failures. The flight tests were conducted at Tomoka RC Flying Club on a day with partly cloudy sky, with a maximum wind speed of 11mph. The details of the flight tests are outlined in Appendix 1.

Among the few possible reasons for the MFC-actuated ailerons to not perform as expected are insufficient blocking force and insufficient lift due to using having half an aileron and with reduced deflection angles. The proposed solution is to remodel MFC-actuated ailerons into full-sized ailerons. The current design restricts the allowable aileron deflection as the glass weave substrate that holds the MFCs are attached partly onto the foam wing and the foam aileron. In order to fully utilize the maximum achievable deflection of the MFC itself, it is recommended to remove the foam along the wing span that contains the aileron structure and replace it with a carbon fiber shell that mimic part the airfoil camber that holds only the edge of MFC actuator while allowing the amplifiers for the MFCs being stored within the empty space of the shell. The curves on the trailing edge of the carbon fiber shell is designed to allow

the MFC actuators to achieve their maximum deflection angles. The full airfoil shape can be achieved through the use of latex materials wrapped around the carbon fiber shell and the MFC actuators. This design, which is illustrated in Figure 6.1, does not only make space for more payload but also reduce the overall weight of the aircraft through the use of carbon fiber shell and latex sheets in place of solid foam structure.

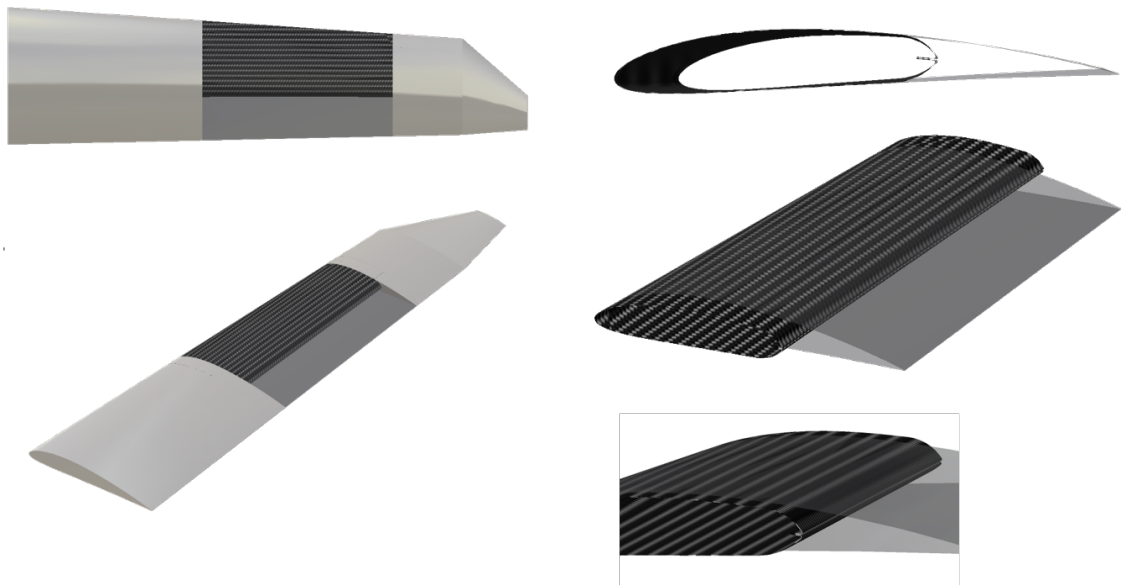


Figure 7.1. Proposed Design for MFC-Actuated Ailerons

Once the prototype is built, the new structure should be wind-tunnel tested for its dynamic coefficients and incorporate them into the simulation that is constructed in this thesis and future flight testing if there is improvement in actuator performance.

REFERENCES

- Barbarino, S., Bilgen, O., Ajaj, R. M., Friswell, M. I., & Inman, D. J. (2011). *A re-view of morphing aircraft* (Vol. 22 ed.). journals.sagepub.com/home/jim: Journal of Intelligent Material Systems and Structures.
- Center, L. R. (2000). *Macro-fiber composite (mfc) actuator*. Langley Research Center.
- Chan, M. C., Moncayo, H., Perez, A., Prazenica, R., Kim, D., & Azizi, B. (2014). *Development and testing of an unmanned aerial system with macro-fiber composite actuators*. American Institution of Aeronautics and Astronautics.
- Corp., S. M. (2017). *Mfc engineering properties*. Smart Material Corp.
- Creech, G. (2012). *Intelligent control for performance: Reducing drag, saving fuel*. NASA Dryden Flight Research Center.
- Flexsys. (2017). *Flexfoil^{FM} compliant control surfaces*. Flexsys.
- Gao, X., Shih, E., & Shih, W. (2009). *Induced voltage of piezoelectric unimorph cantilevers of different nonpiezoelectric/piezoelectric length ratios* (Vol. 18 ed.). Smart Mater. Struct.
- Hartley, R. F., Hugon, F., & DeRosa, B. (2012). *Development and flight testing of the ardupilot 2.0 simulink blockset for a small unmanned aircraft*. Gulfstream Aerospace Corporation.
- Moncayo, H., Perhinschi, M. G., Wilburn, B., Wilburn, J., & Karas, O. (2012). *Extended nonlinear dynamic inversion control laws for unmanned air vehicles*. American Institute of Aeronautics and Astronautics.
- Needham, C. J., & Boyle, R. D. (2003). *Performance evaluation metrics and statistics for positional tracker evaluation*. Heidelberg Berlin: Springer-Verlag.
- StartupBoeing. (2007). *The 737-300/-400/-500*. The Boeing Company.
- Wang, Q., & Cross, L. (1998). *Induced voltage of piezoelectric unimorph cantilever bending actuators* (Vol. 18 ed.). Ferroelectrics.
- Wang, Q., & Cross, L. (1999). *Constitutive equations of symmetrical triple layer piezoelectric benders*. Institute of Electrical and Electronics Engineers.
- Wen, J., & Balas, M. (1989). *Robust adaptive control in hilbert space* (Vol. 143 ed.). Math Analysis Application.

A. Skywalker Pre-flight Checklist

Date and Time of Flight: 04/10/2015 (Friday), 6:00PM Objective(s): Skywalker with MFC-actuated ailerons flight test Weather: Partly cloudy with a maximum wind speed of 11mph Lab Attendees: May, Willies

General Notes 1. Send out pre-flight checklist to Dr. Moncayo 2 days before schedule flight. 2. A test log shall be maintained with the following minimum information: Date, time, active participants, vehicle configuration, vehicle mass, objective, results, anomalies, and notes. 3. Before the test ensure the transmitters have the proper PWM range and channel configurations.

Pre-Test 1. Verify main power batteries are disconnected from the vehicle's power busses. 2. Perform a configuration check of the vehicles systems and verify components and connections are as-expected. 3. Perform mechanical inspection of the vehicle and verify structures and mechanisms appear in good working order. 4. Verify propellers are tight, i.e. cannot spin with respect to motor's rotor under hand-applied torque. 5. Verify motors attachments are tight and that the thrust vector of each motor is at zero degrees inclination. 6. Verify battery voltages are sufficient for flying (18V for motors, 5V for avionics). 7. Perform any test-specific mechanical and electrical connections as-required. DO NOT connect vehicle batteries at this time.

8. Inspect vehicle and adjacent area for FOD and remove as-required. 9. Conduct safety and task briefings for test team personnel.

Vehicle Power Up 1. Upload last version of the control system code to the APM. 2. Arm APM for data recording if there is an intention of saving data from APM sensors. 3. Power up APM before unplugging the USB cable. 4. Turn on transmitter and wait for board to calibrate (solid blue LED indicates GPS lock). 5. Verify that the power LED is solidly lit in orange. 6. Clear all personnel off the takeoff runway, with the exception of RC pilot and the person who helps the airplane takeoff. 7. Make sure that all control sticks on the pilot transmitter are in neutral or zero position. 8. Power up motor battery for propellers.

Vehicle in Air (Flight Test Maneuvers) 1. Speeding up and slowing down change speed while maintaining constant altitude and heading. Pick a few speeds as desired and stabilize airplane at each speed. 2. Turns deflect the rudder towards the inside of the turn (to compensate for long-tail slip effect), and then deflect the ailerons toward the outside of the turn (to compensate for overbanking tendency). 3. Coordinated wing rocking roll rather rapidly into a 45 bank to the left. Pause for a moment, then roll to wings level. Pause again, and then roll 45 to the right. Pause again, roll wings level, and repeat 2-3 times (to learn about the airplanes roll-wise inertia and adverse yaw). 4. Constant-heading slips put the airplane in a slight bank (15), then apply top rudder to keep it from turning. Hold it there for a few seconds, then roll back to wings level. Hold it there, and then roll to the other side, maintaining constant heading throughout (to feel the control and response of the aircraft). Note:

maneuvers to be conducted on both of the mechanical and MFC-actuated ailerons.

Vehicle Power Down 1. Turn off flight system batteries. 2. Check for damage. Note down damages if any.

Emergency Procedures 1. Call Dr. Hever Moncayo at XXX-XXX-XXXX in case of injury to personnel, battery fire, or severe damage to facilities.